Influence of dilatancy on the frictional constitutive behavior of a saturated fault zone under a variety of drainage conditions

Jon Samuelson,[1,2] Derek Elsworth,[1] and Chris Marone[1]

Received 30 May 2011; accepted 21 July 2011; published 18 October 2011.

[1] We use numerical simulations to investigate how fault zone dilatancy and pore fluid decompression influence fault strength and friction constitutive behavior. Dilatant hardening can change the frictional response and the effective critical stiffness, K_{cr}, which determines the transition from stable to unstable sliding in velocity weakening fault zones. We study the frictional shear strength response to numerical velocity stepping experiments and show that when the duration of pore fluid decompression is long compared to the time necessary for frictional evolution (as dictated by rate and state friction) both the effective critical slip distance (D_C') and the effective shear strength direct effect (A') are increased. We investigate the role of fault zone permeability (k), dilatancy coefficient (ε), and the magnitude of shearing velocity of the fault zone (v_{lp}) and compare results using the Dieterich and Ruina state evolution laws. Over the range from $k = 10^{-15}$ to 10^{-21} m^2, D_C' increases from 25 μm to ~2 mm and A' increases from 0.15 to ~5 MPa. We vary ε from 10^{-5} to 10^{-3} and the size of the velocity perturbation from 3X to 1000X and find large increases in the values of D_C' and A', which may lead to inhibition of unstable sliding. Our results indicate that spatial variations, with either depth or lateral extent, in ε and k could result in significant changes in the drainage state in fault zones. Such variation may lead to spatial variation of the nucleation and propagation of earthquakes based upon the drainage capabilities of the fault zone.

Citation: Samuelson, J., D. Elsworth, and C. Marone (2011), Influence of dilatancy on the frictional constitutive behavior of a saturated fault zone under a variety of drainage conditions, *J. Geophys. Res.*, *116*, B10406, doi:10.1029/2011JB008556.

1. Introduction

[2] The shear strength (τ) of elastic surfaces in frictional contact may be represented as

$$\tau = \mu\sigma', \tag{1}$$

where μ is the coefficient of friction and σ' is the effective normal stress. Effective stress is a function of the applied normal stress (σ_n) and the pore fluid pressure at the interface of the surfaces (P_P) [e.g., *Hubbert and Rubey*, 1959]:

$$\sigma' = \sigma_n - P_P. \tag{2}$$

Equations (1) and (2) show that shear strength is a function of both the coefficient of friction (μ) and the pore pressure (P_P) at the interface. If P_P changes, either through dilatancy-induced depressurization of the pore fluid or shear heating, the effective stress will increase or decrease, respectively, leading to an increase or decrease in shear strength. Similarly, if μ changes, for example as a function of shearing velocity or contact aging, the shear strength of the contact changes.

[3] The rate- and state-dependent friction laws were developed to describe the evolution of friction in response to changes in shearing velocity, much like those resulting from an earthquake. The rate and state law [*Dieterich*, 1979, 1981; *Ruina*, 1983],

$$\mu = \mu_0 + a\ln\left(\frac{v}{v_0}\right) + b\ln\left(\frac{v_0\theta}{D_C}\right), \tag{3}$$

describes the evolution of friction away from a steady state value (μ_0), in response to a change in sliding velocity from the background value (v_0) to a new value (v) over a critical slip distance (D_C). The state variable (θ), thought of as the average life span of a set of frictional contacts, also evolves over the sliding distance D_C in response to the change in sliding velocity from v_0 to v, according to one of two state evolution laws: the Dieterich (or Aging) Law,

$$\frac{d\theta}{dt} = 1 - \frac{v\theta}{D_C'}, \tag{4}$$

[1]Rock and Sediment Mechanics Laboratory, Center for Geomechanics, Geofluids, and Geohazards, and Energy Institute, Pennsylvania State University, University Park, Pennsylvania, USA.
[2]Now at Faculty of Geosciences, HPT Laboratory, Utrecht University, Utrecht, Netherlands.

Copyright 2011 by the American Geophysical Union.
0148-0227/11/2011JB008556

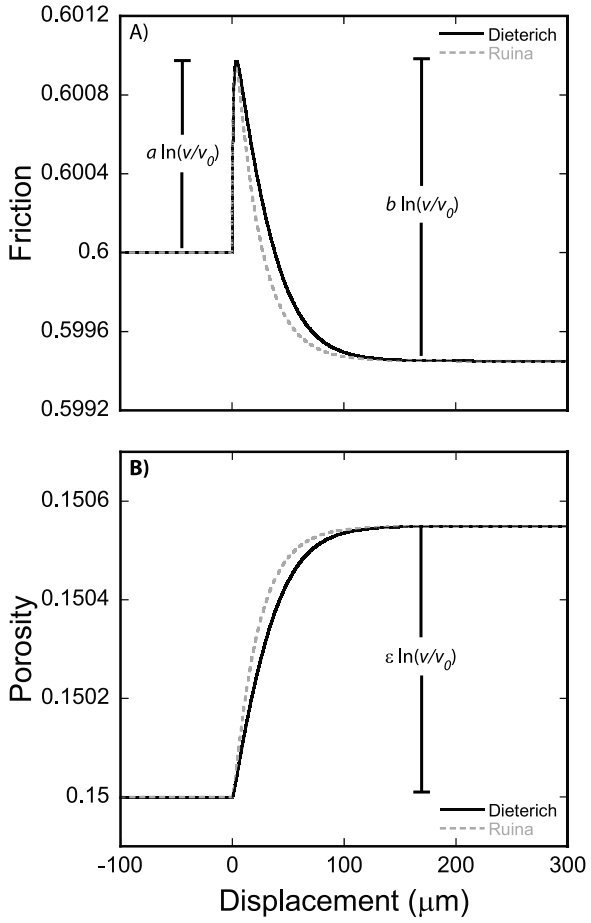

Figure 1. (a) Frictional response to a change in sliding velocity from 10 μm/s to 30 μm/s as described by the rate- and state-dependent friction law equation (3), using both Dieterich and Ruina style state evolution. The magnitude of the increase and subsequent decay in friction resulting from the velocity step are controlled by the magnitude of the velocity step; the direct effect, a = 0.001; the evolution effect, b = 0.0015; the evolution occurs over roughly the critical slip distance, D_C = 25 μm. (b) Porosity evolves similarly in response to the increase in shear velocity, controlled by the magnitude of the velocity increase, and the dilatancy coefficient, $\varepsilon = 5 \times 10^{-4}$.

or the Ruina (or Slip) Law,

$$\frac{d\theta}{dt} = -\frac{v\theta}{D_C}\ln\left(\frac{v\theta}{D_C}\right). \tag{5}$$

At steady state $d\theta/dt = 0$, and for both state evolution laws $\theta_{ss} = D_C/v$. If v is larger than v_0 (Figure 1a), then the response will be an immediate increase in friction, followed by a decay over the critical slip distance D_C to a new steady state value. The magnitude of the increase and subsequent decay in friction are controlled by the terms $a\ln(v/v_0)$ and $b\ln(v/v_0)$, respectively. In the case shown in Figure 1a, μ_0 = 0.6, a = 0.001, b = 0.0015, v_0 = 10 μm/s, v = 30 μm/s, and D_C = 25 μm. In this example the parameter a-b is negative, resulting in so-called "velocity-weakening" behavior, where $\mu < \mu_0$; this is a necessary condition for unstable stick-slip sliding on a fault zone.

[4] In a fault zone, porosity also evolves from one steady state value to another, due to changes in sliding velocity [e.g., *Marone et al.*, 1990; *Segall and Rice*, 1995; *Samuelson et al.*, 2009]. Like friction, porosity (ϕ) appears to evolve over a distance approximately equal to D_C, and follows the equation

$$\phi = \phi_0 - \varepsilon \ln\left(\frac{v_0\theta}{D_C}\right), \tag{6}$$

where ϕ_0 is initial porosity, ε is a dilatancy coefficient, and θ evolves as either the Dieterich (equation (4)) or Ruina (equation (5)) state evolution laws [*Segall and Rice*, 1995]. Using $\varepsilon = 5 \times 10^{-4}$ [*Samuelson et al.*, 2009], Figure 1b shows the porosity response to a step in shearing velocity from 10 to 30 μm/s. The magnitude of the porosity increase is determined by ε and the size of the velocity step. In the case of a completely drained fault zone, the changes in porosity associated with changes in shearing velocity will not result in any change in the effective stress, and therefore the change in shear strength of the fault zone will track the change in friction as it evolves from μ_0 to μ. However, if the rate of dilation exceeds the rate of fluid flow into the fault zone, the pore fluid will decompress, leading to increased effective stress and shear strength, potentially inhibiting the nucleation of earthquake slip [*Scholz*, 1988a; *Sleep*, 2006; *Barbot et al.*, 2008; *Rubin*, 2008; *Brantut et al.*, 2010; *Segall et al.*, 2010; *Tanikawa et al.*, 2010]. Previous works show that permeability of fault gouge can vary from 10^{-14} m^2 at low confining stresses to 10^{-21} m^2 at seismogenic depths [*Wibberley*, 2002; *Mitchell and Faulkner*, 2008], a variation that could result in a spectrum from quasi-drained to quasi-undrained conditions. In addition to the magnitude of the velocity increase, the size of the dilatancy coefficient also plays a role in the drainage state of a fault zone by controlling the rate of pore volume creation. Laboratory measurements for granular fault gouge show that ε is in the range of 10^{-5} to 10^{-3} [*Marone et al.*, 1990; *Samuelson et al.*, 2009].

[5] For a tectonic fault zone, the evolution of shear stress following a perturbation in shear stress or slip velocity depends on the fluid pressure and state of drainage. In the undrained case, dilatant hardening will combine with rate/state friction response to produce a complex behavior in which shear strength evolution depends on frictional state evolution, dilation, and fluid flow. A decrease in pore pressure may result in a significant increase in the frictional yield strength, leading to an effective increase in the direct effect. Moreover, the effective value of the critical slip distance D_C' will increase if the time necessary for full drainage of the fault zone is long compared to the time necessary for friction state evolution.

[6] In addition to the role of dilatancy and frictional evolution in determining shear strength, many recent studies have focused on the importance of frictional shear heating, in order to better understand the complex processes that control earthquake nucleation and coseismic slip [*Sleep*, 1995; *Andrews*, 2002; *Bizzarri and Cocco*, 2006a, 2006b; *Rice*, 2006; *Segall and Rice*, 2006; *Brantut et al.*, 2008,

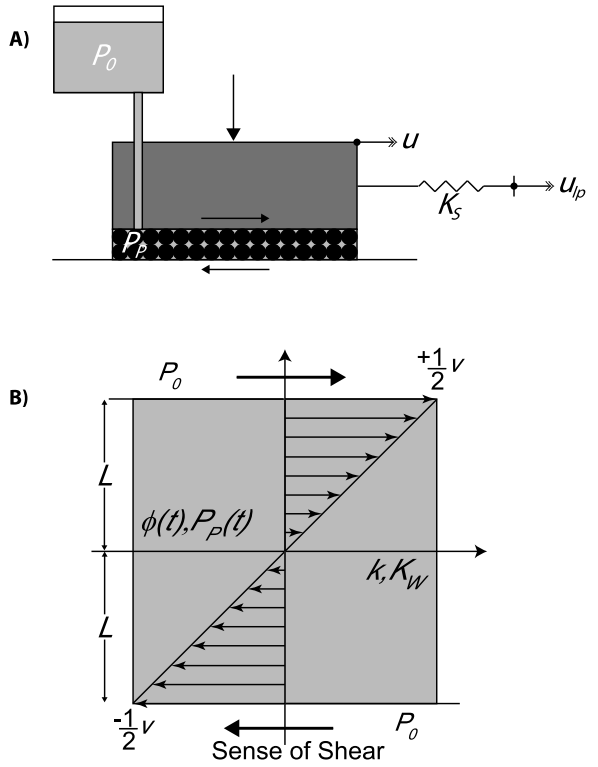

Figure 2. (a) Schematic poromechanical representation of our fault model. The shaded region represents a fault block with displacement u subjected to normal stress σ_n in contact with a granular fault zone with internal pore pressure, P_P. The fault zone is connected to an external reservoir at pore pressure P_0. At steady state $P_P = P_0$. The fault block is connected to a load point by a spring of stiffness K_S. Shear stress, τ, is measured at the load point. Sense of shear is top to the right. (b) Schematic of the sheared fault zone. Shear, and therefore dilation, is assumed to be evenly distributed across the thickness of the layer ($2L$). P_0, fluid compressibility (K_W), and permeability (k) are presumed to be constant, while porosity (ϕ), and internal pore pressure (P_P) are time-dependent.

2010; *Bizzarri*, 2009; *Liu and Rubin*, 2010; *Nielsen et al.*, 2010; *Segall et al.*, 2010; *Ujiie and Tsutsumi*, 2010; *Rubin*, 2011]. *Segall and Rice* [2006] predict nearly complete shear decoupling of a fault zone with an initial shear strength of ~80 MPa as a result of shear heating, inferring a net 130 MPa increase in pore pressure. *Bizzarri and Cocco* [2006b] argue that the importance of dilatancy to the overall strength evolution of a fault zone during nucleation is relatively small. They show that the pore pressure evolution in a nondilatant, thermally pressurized fault zone is ultimately very similar to that in a dilatant, thermally pressurized fault zone, differing only by a small amount when the rate of pore volume creation is at its maximum. Of course, the values used for the dilatancy rate play an important role in such model studies. Our model results, coupled with our laboratory measurements of diltancy [*Samuelson et al.*, 2009] show that dilatancy's contribution to pore pressure change may be much larger than predicted by *Bizzarri and Cocco* [2006a, 2006b].

[7] The purpose of this paper is to examine the influence of dilatancy and fluid decompression on the frictional properties of a fluid-saturated fault zone. We focus on faults with complex, realistic friction constitutive behavior such as that described by the rate and state friction laws. Sensitivity analyses are conducted to represent experimental conditions replicated in the Penn State triaxial apparatus [*Ikari et al.*, 2009; *Samuelson et al.*, 2009; *Faoro et al.*, 2009] and representative of constitutive parameters consistent with a fault zone at ~10 km depth. Correspondingly, we examine the functional alteration of the friction constitutive parameters, absent consideration of shear heating, in order to focus on the role of dilation and fluid flow.

[8] In some ways the work presented here is similar to previous numerical studies on the role of dilatancy in fault zones, in particular the ability of pore fluid decompression to stabilize fault zones by transiently increasing shear strength [*Garagash and Rudnicki*, 2003a, 2003b; *Hillers et al.*, 2006; *Hillers and Miller*, 2006; *Segall et al.*, 2010]. Our work differs from that of *Garagash and Rudnicki* [2003a, 2003b] by way of our implementation of rate- and state-dependent frictional behavior, rather than slip-weakening behavior alone, which allows us to investigate the full evolution of shear strength in a fault zone with controlled fluid drainage parameters. Additionally, our work differs from the studies of *Hillers et al.* [2006] and *Hillers and Miller* [2006] in that our intention is to analyze specifically the effective change in rate and state constitutive parameters resulting solely from fault zone dilatancy. To do this, we use a numerical simulation of a laboratory experiment performed under the in situ conditions of a natural fault zone. We use the numerical experiments to focus on the interplay dilatancy and drainage exert on the evolution of "effective" rate-state constants and bounds of these the effects of dilatant hardening for these effective parameters.

2. Constitutive Model

[9] For a deforming fault zone, the rate/state friction response is governed by two coupled differential equations. The first involves state evolution $d\theta/dt$, for which we can either use equation (4) or equation (5), and the second is elastic coupling between the fault and its surrounding, which can be written as $d\mu/dt$, in the case of a simple spring-slider model (Figure 2a). We represent the fault as a spring-slider system composed of a linear spring of stiffness K_S activated by a load point moving at constant velocity, v_{lp}, the displacement of which is u_{lp}. Differential displacement between the load point and slider generates shear stress (τ) as

$$\tau = K_S\left(u_{lp} - u\right), \tag{7}$$

where u is the displacement of the slider. Equation (7) is Hooke's law, and if we divide both sides by σ', and take the time derivative, we obtain

$$\frac{d\mu}{dt} = \frac{K_S}{\sigma'}\left(v_{lp} - v\right), \tag{8}$$

where v_{lp} and v are the load point velocity and slider velocity, respectively, and $d\mu/dt$ is the elastic interaction term commonly used to solve the rate and state friction law.

[10] Equations (5)–(8) are sufficient in cases where neither K_S, nor σ' are functions of time; however, in the case of a saturated, quasi-impermeable fault zone, σ' *is* time-dependent, due to the transient decompression of the pore fluid [e.g., *Rice and Rudnicki*, 1979; *Rudnicki and Chen*, 1988; *Segall and Rice*, 1995; *Barbot et al.*, 2008]. In such cases, the time derivative of

$$\tau = \mu(\sigma_n - P_P) = K_S\left(u_{lp} - u\right), \tag{9}$$

results in an elastic coupling term where

$$\frac{d\mu}{dt} = \frac{K_S}{(\sigma_n - P_P)}\left(v_{lp} - v\right) + \frac{\mu}{(\sigma_n - P_P)}\frac{dP_P}{dt}. \tag{10}$$

In this case it is clear that in addition to solving $d\theta/dt$, and $d\mu/dt$, we must also now solve dP_P/dt.

[11] To obtain an equation for dP_P/dt, we must include a term based on the rate of plastic pore volume creation, which allows for decompression of pore fluid, a term based on the diffusion of pore fluid into the fault zone, allowing the pore pressure to return to an equilibrium value, and finally a term allowing the pore volume, and therefore fluid pressure, to change elastically in response to changes in effective stress [e.g., *Segall and Rice*, 1995]:

$$\frac{dP_P}{dt} = \left(\frac{dP_P}{dt}\right)_{plastic} + \left(\frac{dP_P}{dt}\right)_{drainage} + \left(\frac{dP_P}{dt}\right)_{elastic}, \tag{11}$$

which we can then express in mechanical terms as

$$\frac{dP_P}{dt} = \frac{dP_P}{dV_f}\left[\left(\frac{dV_f}{dt}\right)_{plastic} + \left(\frac{dV_f}{dt}\right)_{drainage} + \left(\frac{dV_f}{dt}\right)_{elastic}\right], \tag{12}$$

where V_f is the fluid volume. The term outside of the brackets (dP_P/dV_f) can be obtained by rearranging the bulk modulus of water (K_W):

$$\frac{dP_P}{dV_f} = \frac{-K_W}{V_f}. \tag{13}$$

[12] The first term inside of the brackets describes the decompression of the pore fluid, which can be obtained by taking the time derivative of equation (6):

$$\left(\frac{dV_f}{dt}\right)_{plastic} = V_T\frac{d\phi}{dt} = AL\left(\frac{-\varepsilon}{\theta}\frac{d\theta}{dt}\right), \tag{14}$$

where A is the cross-sectional area of interest and L is the half-thickness of the gouge layer, combining as the half-volume of the gouge layer, V_T.

[13] We use a quasi-steady approximation for fluid flow into the layer ($\left(\frac{dV_f}{dt}\right)_{drainage}$) with the flow rate proportional to the instantaneous pressure difference between fault perimeter and fault core, rather than accommodating the full transient flow [*Samuelson et al.*, 2009]. This allows us to calculate a fluid pressure that is averaged over the thickness of the fault zone and also simplifies our final differential equations. Therefore for volume flow rate we use

$$\left(\frac{dV_f}{dt}\right)_{drainage} = Q = -A\frac{k}{\eta}\frac{(P_P - P_0)}{L}, \tag{15}$$

where A is the area through which the fluid flow takes place, η is the dynamic fluid viscosity, k is the permeability of the fault zone gouge, P_P is the internal fault zone fluid pressure, P_0 is a remote pore pressure external to the fault zone, and L is again the fault zone half-thickness.

[14] The final term inside of the brackets of equation (12) deals with the elastic compressibility of the pore volume. We couple the compressibility of the pore volume with the rate of change of fluid pressure to arrive at the rate of change of fluid volume due to pore compressibility:

$$\left(\frac{dV_f}{dt}\right)_{elastic} = \frac{dP_P}{dt}\frac{dV_\phi}{dP_P} = \frac{dP_P}{dt}\left(V_f\beta_\phi\right), \tag{16}$$

where β_ϕ is the pore compressibility of the fault core, and acknowledging that the pore volume V_ϕ, and fluid volume V_f are equivalent. Combining the terms from equations (13)–(16) leads to a final differential equation for the rate of change of fluid pressure in a partially drained, dilatant fault zone:

$$\frac{dP_P}{dt} = \frac{\left(\frac{\varepsilon}{\theta}\frac{d\theta}{dt}\right) + \left(\frac{k}{\eta L^2}\left(P_P - P_{P0}\right)\right)}{\phi\left(\beta_W + \beta_\phi\right)}, \tag{17}$$

which acknowledges that the fluid volume in the half-layer is equal to the product of the area (A), the layer half-thickness (L), and the porosity of the fault zone (ϕ).

[15] Once we solve equation (3) for v, we have a full set of differential equations, conceptualized in Figure 2b, that can be solved to obtain μ, and P_P (and therefore τ) of a dilatant fault zone subjected to a sudden increase in shear velocity, as during the nucleation phase of an earthquake:

$$\left.\begin{aligned}
v &= \frac{du}{dt} = v_0\exp\left\{\frac{1}{a}\left[(u - u_0) - b\ln\left(\frac{v_0\theta}{D_C}\right)\right]\right\}\\
\frac{d\theta}{dt} &= 1 - \frac{v\theta}{DC} \quad or \quad \frac{d\theta}{dt} = -\frac{v\theta}{D_C}\ln\left(\frac{v\theta}{D_C}\right)\\
\frac{d\mu}{dt} &= \frac{K_S}{(\sigma_n - P_P)}\left(v_{lp} - v\right) + \frac{\mu}{(\sigma_n - P_P)}\frac{dP_P}{dt}\\
\frac{d\phi}{dt} &= \frac{-\varepsilon}{\theta}\frac{d\theta}{dt} + \phi\beta_\phi\frac{dP_P}{dt}\\
\frac{dP_P}{dt} &= \frac{\left(\frac{\varepsilon}{\theta}\frac{d\theta}{dt}\right) + \left(\frac{k}{\eta L^2}\left(P_P - P_{P0}\right)\right)}{\phi\left(\beta_\phi + \beta_W\right)}
\end{aligned}\right\}. \tag{18}$$

We solve these coupled equations using a modified fifth-order Runge-Kutta-Fehlberg method with error tolerance between 1×10^{-6} and 5×10^{-4}. Then, using the effective stress law (equation (1)), we obtain the shear strength of the fault zone as a function of changes in both friction coefficient and pore pressure.

[16] Once we obtain solutions to equation (18), we invert the model output using a Levenberg-Marquardt least squares approach to obtain a best fit estimate of the rate and state friction constitutive parameters [e.g., *Blanpied et al.*, 1998; *Mair and Marone*, 1999; *Frye and Marone*, 2002, *Ikari et al.*, 2009]. The results of this inversion are effective values of the rate/state friction parameters A' and D_C', which correspond to the standard constitutive parameters A (= $a\sigma'$) and D_C. The use of the effective constitutive parameters, A'

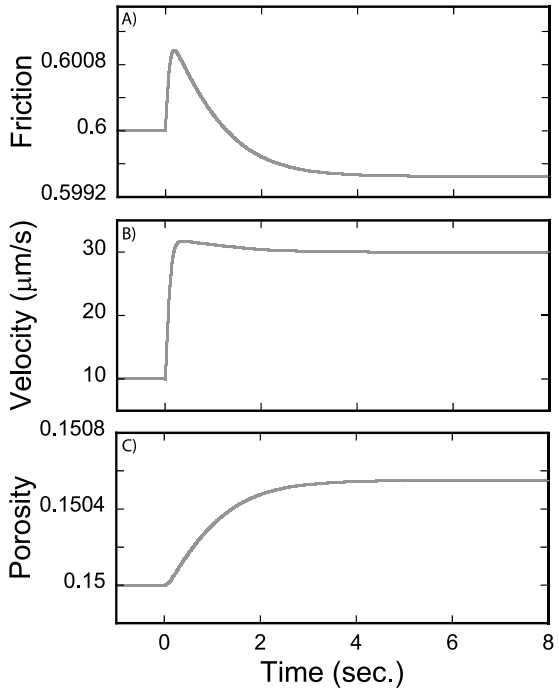

Figure 3. (a) Frictional response to 10–30 μm/s velocity step as a function of time, where $a = 0.001$, $b = 0.0015$, $D_C = 25$ μm. (b) Time series of fault velocity. Acceleration is not instantaneous, but rather a function of the elastic coupling between the load point and the fault. (c) Porosity response of the fault zone to the 10–30 μm/s velocity step as a function of time. $\varepsilon = 5 \times 10^{-4}$.

and D_C', explicitly acknowledges that the effective shear strength response will be the combined effect of the intrinsic friction behavior and the poromechanical behavior.

3. Results

[17] We begin by considering the effects of changing the permeability (k), dilatancy coefficient (ε), and load point velocity step (v_{lp}) on the pore pressure and hence shear strength of dilatant fault zones. Decreases in k and increases in ε and v_{lp} should lead to more thorough decompression of the pore fluid and larger increases in the values of A′ and D_C'.

[18] In all model experiments we use the same basic parameters, while varying permeability (k), dilatancy coefficient (ε), and load point velocity (v_{lp}) step size. The constants we use are based on field evidence, experimental analysis, known machine values of the Penn State biaxial apparatus, and are roughly appropriate for a depth of ~10 km and a temperature of 250°C. The constants we use are as follows: $\mu_0 = 0.6$ [*Byerlee*, 1978], $\phi_0 = 0.05$ [*Wibberley et al.*, 2008], $v_0 = 10$ μm/s, $D_C = 25$ μm [*Marone*, 1998], $a = 0.001$ and $b = 0.0015$ [*Marone et al.*, 1990; *Mair and Marone*, 1999; *Ikari et al.*, 2009], $K_S = 0.1$ MPa/μm (measured stiffness of Penn State load frame), $B_W = 6.87 \times 10^{-4}$ MPa^{-1} (water compressibility) [*Wagner and Pruss*, 2002], $B_P = 5.0 \times 10^{-4}$ MPa^{-1} (pore compressibility) [*Rice*, 2006], $\sigma = 250$ MPa, $P_0 = 100$ MPa, $\eta = 1.28 \times 10^{-10}$ MPa·s (dynamic viscosity of water) [*Harvey and Friend*, 2004], and finally $L = 3000$ μm [*Wibberley and Shimamoto*, 2003]. With $\mu = 0.6$ and $\sigma' = 150$ MPa, the initial steady state shear strength of our simulated fault zone is 90 MPa.

[19] In order to vary the drainage state of the simulated fault zone we systematically alter the permeability (k) from 10^{-15} to 10^{-21} m^2 based on previous works [*Wibberley*, 2002; *Wibberley and Shimamoto*, 2003, *Wibberley et al.*, 2008; *Mitchell and Faulkner*, 2008; *Tanikawa et al.*, 2010], the dilatancy coefficient (ε) from 10^{-5} to 10^{-3} [*Marone et al.*, 1990; *Samuelson et al.*, 2009; J. Samuelson and C. Marone, Laboratory measurements of the frictional dilatancy coefficient for natural and simulated fault zones manuscript in preparation, 2011], and the load point velocity (v_{lp}) from 10 to 30, 100, 300, and 1000 μm/s to simulate the velocity stepping experiments of the Penn State biaxial/triaxial apparatus [e.g., *Mair and Marone*, 1999; *Ikari et al.*, 2009; *Samuelson et al.*, 2009]. *Hillers and Miller* [2006] point out that the dilatancy measurements of *Marone et al.* [1990] were done at slip velocities within the realm of the nucleation of dynamic slip (1–10 μm/s), and subsequently surmised that ε may be far smaller at the lower velocities more typical at nucleation. Contrary to that notion, the more recent experiments of *Samuelson et al.* [2009], which measured the dilatancy coefficient over a range of velocity step sizes from 1 to 100 μm/s showed no strong correlation between velocity and ε, suggesting that using a dilatancy coefficient on the order of 5×10^{-4} is appropriate for those simulations in which ε is not the control variable. The experiments of *Samuelson et al.* [2009] were, however, conducted at much lower effective stresses than those simulated here, and therefore ε could be different at higher effective stress, though these experiments showed no consistent variation of ε based on normal stress. Moreover, the experiments of *Marone et al.* [1990] were conducted at $\sigma' = 150$ MPa and showed a dilatancy coefficient within the range used in our simulations.

[20] A time series using the Dieterich state evolution law (Figure 3) shows evolution of μ, v, and ϕ in response to a change in the load point velocity from 10 to 30 μm/s in a completely drained fault zone. Friction increases from 0.6 to approximately 0.601 and then evolves to 0.5995, and porosity evolves from 0.15 to 0.1506. Note that the evolution of the shearing velocity of the fault zone from 10 to 30 μm/s is not instantaneous due to elastic coupling, and for the parameters used, we find a slight overshoot in velocity, such that $v > 30$ μm/s, which can be seen both in Figure 3 and in model results presented below. In all cases, models were run until key variables (μ, ϕ, and P_P) reached steady state. The time necessary to reach steady state is controlled by friction evolution in cases where pore fluid decompression is insignificant or by the pore pressure evolution in other cases.

3.1. Variable Permeability

[21] Using $\varepsilon = 5 \times 10^{-4}$ and $v_{lp} = 30$ μm/s, we explored a range of fault permeabilities from 10^{-15} to 10^{-21} m^2 using both the Dieterich and Ruina (Figure 4) state evolution laws. Both laws show that for low fault zone permeability the depressurization of pore fluid and associated shear strengthening is significant. Using the Dieterich law and $k \geq 10^{-17}$ m^2, we find a very small reduction in pore fluid pressure (<0.1 MPa) (Figure 4a). For $k < 10^{-17}$ m^2 the fault zone is progressively more depressurized as permeability decreases. In these cases the rate of pore volume creation exceeds the rate of fluid flow

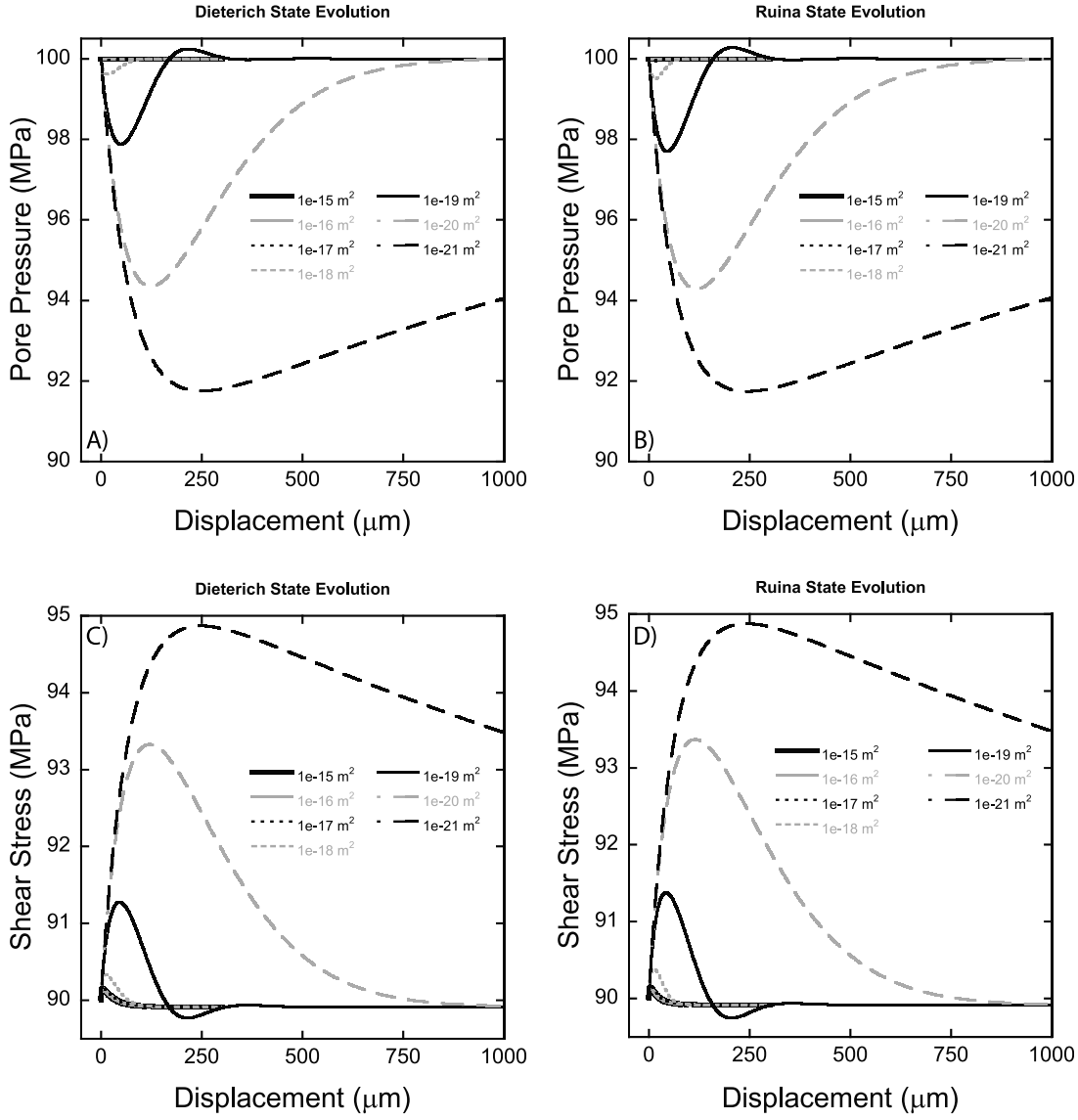

Figure 4. Effect of permeability (k) on (a, b) pore pressure and (c, d) shear strength evolution as a result of a threefold velocity step in a fault zone with a half-thickness of 3 mm. Figures 4a and 4c are for Dieterich style state evolution and Figures 4b and 4d are for Ruina state evolution. In all cases $v_0 = 10$ μm/s, $v_{lp} = 30$ μm/s, $a = 0.001$, $b = 0.0015$, $D_C = 25$ μm, $\varepsilon = 5 \times 10^{-4}$, $\sigma_n = 250$ MPa, $P_0 = 100$ MPa.

into the fault zone. At $k = 10^{-18}$ m^2 the maximum depressurization of the fault zone is 0.39 MPa, and this value increases to 8.2 MPa at $k = 10^{-21}$ m^2.

[22] For a fluid saturated fault, the evolution of shear strength, $\tau = \mu(\sigma_n\text{-}P_P)$, with slip varies with fault zone permeability (Figure 4b). Where the permeability is relatively large ($k \geq 10^{-17}$ m^2), and therefore the reduction in pore pressure small, the maximum shear strength of the fault zone is 90.2 MPa for our model parameters. Here we see that the evolution of shear stress behaves very nearly as it would under completely drained conditions, with the shear stress evolving, as does friction, over the sliding distance D_C. The increase in shear strength is controlled by the friction direct effect ($A = a\sigma'$).

[23] As the permeability of the shear zone decreases, the evolution of shear strength transitions from being controlled by friction evolution to being controlled by the pore-omechanical factors of fluid depressurization and flow. The increase in shear strength as a result of pore fluid decompression is particularly evident at this scale beginning at $k = 10^{-19}$ m^2, where the shear strength maximum is 91.3 MPa, and increases to a maximum shear strength of 94.9 MPa when the permeability of the fault zone is 10^{-21} m^2 (Figure 4b).

[24] We initially suspected that Ruina state evolution would result in more complete pore fluid depressurization due to the increased rate of pore volume creation that is evident in Figure 4b, and that suspicion was borne out; however, the difference is very subtle (Figures 4c and 4d). At $k \geq 10^{-17}$ m^2 the pore pressure reduction is quite small, consistent with the result for Dieterich state evolution. At lower permeabilities the pore pressure response increases from 0.51 MPa at $k = 10^{-18}$ m^2 to 8.3 MPa where $k = 10^{-21}$ m^2.

[25] As with pore pressure evolution, the difference between the Dieterich and Ruina laws with regard to the

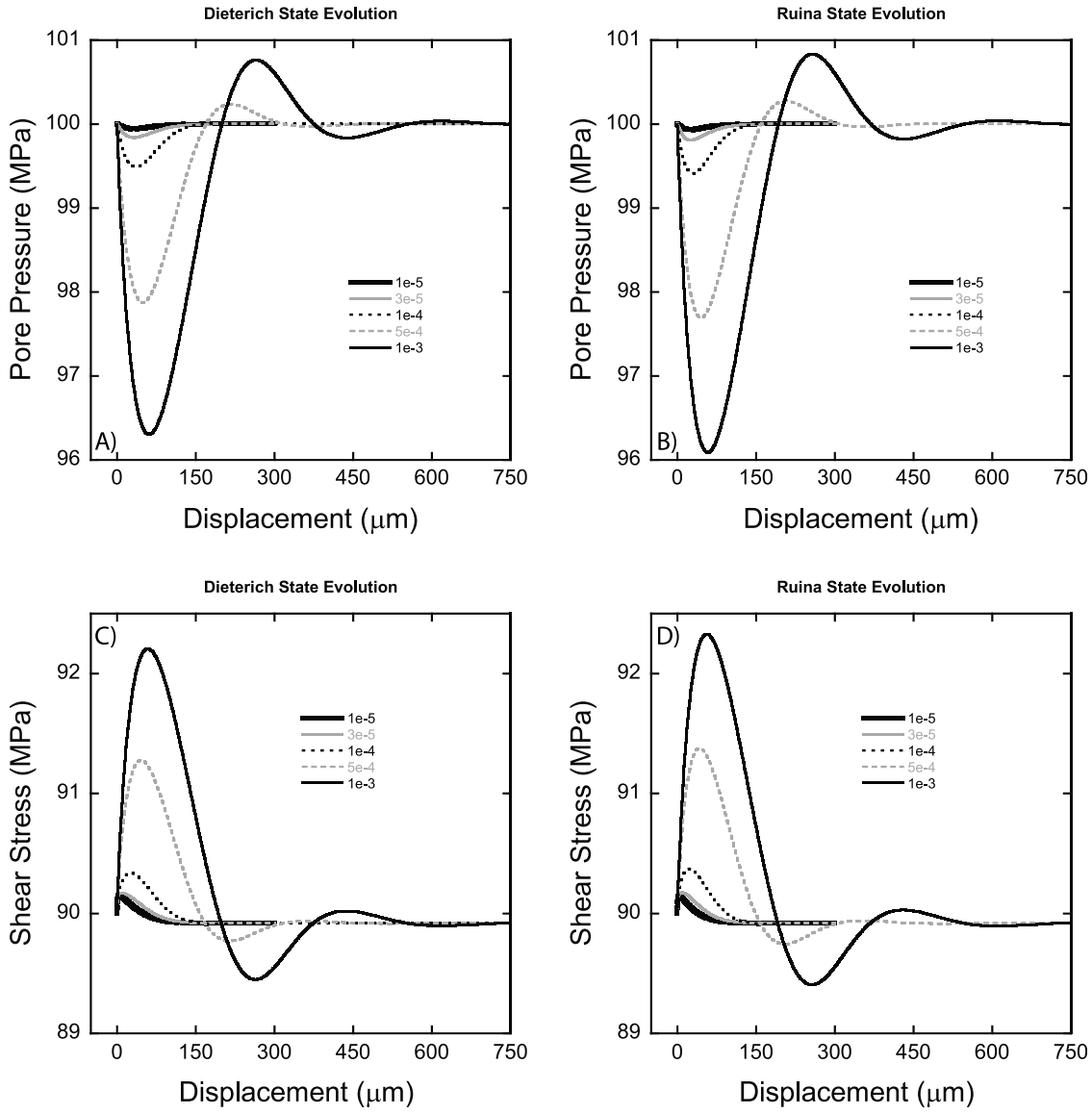

Figure 5. Effect of variable dilatancy coefficient (ε) on (a, b) pore pressure and (c, d) shear strength evolution as a result of a threefold velocity step in a fault zone with a half-thickness of 3 mm. Figures 5a and 5c are for Dieterich style state evolution and Figures 5b and 5d are for Ruina state evolution. In all cases $v_0 = 10$ μm/s, $v_{lp} = 30$ μm/s, $a = 0.001$, $b = 0.0015$, $D_C = 25$ μm, $k = 1 \times 10^{-19}$ m^2, $\sigma_n = 250$ MPa, $P_0 = 100$ MPa.

evolution of shear stress are small. At $k \geq 10^{-17}$ m^2 the peak shear stress is essentially unchanged from what it would be in a completely drained fault zone at a value of 90.17 MPa. At $k < 10^{-17}$ m^2 the peak shear stress begins to be more and more controlled by decompression and subsequent diffusion of pore fluid in the fault zone. At $k = 10^{-18}$ m^2 the peak shear strength is 90.3 MPa, and it is 94.9 MPa when the permeability of the fault zone is 10^{-21} m^2.

[26] Both the Dieterich and Ruina laws result in a fault zone that is very nearly completely undrained when $k = 10^{-21}$ m^2. The undrained pore fluid decompression can be described by the equation

$$\Delta P_{\max} = \frac{-\varepsilon}{\phi_0(\beta_\phi + \beta_W)} \ln\left(\frac{v_0}{v_{lp}}\right). \quad (19)$$

We will discuss $\Delta P_{\max}$ more fully later, but for the present case where $\varepsilon = 5 \times 10^{-4}$, $\beta_W = 6.87 \times 10^{-4}$ MPa^{-1}, $\beta_P = 5.0 \times 10^{-4}$ MPa^{-1}, $\phi_0 = 0.05$, $v_0 = 10$ μm/s, and $v_{lp} = 30$ μm/s, $\Delta P_{\max}$ equals 9.26 MPa, and therefore in the most impermeable case presented here ($k = 10^{-21}$ m^2) the fault zone reaches a level of depressurization of $0.89 \cdot \Delta P_{\max}$.

3.2. Variable Dilatancy Coefficient

[27] On the basis of previous experimental results we varied the dilatancy coefficient (ε) over the range 10^{-5} to 10^{-3} [*Marone et al.*, 1990; *Samuelson et al.*, 2009]. We held permeability constant at 10^{-19} m^2, and all other parameters are identical to those used in section 3.1. Using $k = 10^{-19}$ m^2 results in a reduction in pore fluid pressure at all values of ε for both types of state evolution (Figures 5a and 5c).

[28] Using the Dieterich law, the magnitude of the pore fluid decompression varies from 0.05 MPa where $\varepsilon = 10^{-5}$ to 3.7 MPa at $\varepsilon = 10^{-3}$ (Figure 5a). We can see that when ε is large there is an elastic overshoot of the slider that results in a periodic "ringing" of the pore pressure (and shear stress) around the eventual steady state value. We use the ΔP_{max} term to describe how close to fully undrained the fault zone becomes. This case is slightly more complicated than for variable permeability since ΔP_{max} is different for each different dilatancy coefficient, but it is important to note that the fault zone depressurization is greater than $0.2 \cdot \Delta P_{max}$ in all cases and is actually more fully undrained at lower values for ε, though obviously the overall magnitude of the total depressurization is larger when ε is also large.

[29] When $\varepsilon = 10^{-5}$ the increase in shear strength due to dilatancy hardening is nominal with a maximum shear strength of 90.2 MPa (Figure 5b). When ε is increased to 10^{-3}, dilatancy hardening is much more pronounced, with maximum shear strength reaching 92.2 MPa. Owing to the low permeability of the modeled fault zone in this case, the time necessary for pore fluid to flow into the fault results in a large increase in the effective critical slip distance in all cases.

[30] Comparing the two state evolution styles, we see that Ruina evolution (Figure 5c) results in slightly higher pore fluid decompression and a smaller shear strength increase than the Dieterich law (Figure 5a). At $\varepsilon = 10^{-5}$ the difference between Dieterich and Ruina state evolution is negligible, with a 0.06 MPa reduction in pore pressure. When the dilatancy coefficient is larger ($\varepsilon = 10^{-3}$) the difference between the two evolution styles is more pronounced with pore fluid pressure being reduced by 3.9 MPa for the Ruina law, as opposed to 3.7 MPa using Dieterich evolution.

[31] When $\varepsilon = 10^{-5}$ using the Ruina law peak shear strength is barely higher than in a completely drained scenario, reaching only 90.15 MPa (Figure 5d). When $\varepsilon = 10^{-3}$ the maximum shear strength is increased to 92.3 MPa. There is a clear increase in the effective values of the direct effect and the critical slip distance as ε is increased from 10^{-5} to 10^{-3}. These results illustrate the important relationship between pore fluid pressure reduction and ε, due to the increasing potential for depressurization that results from increased dilatancy.

3.3. Variable Load Point Velocity

[32] A key variable in studies of earthquake nucleation and dynamic rupture is the fault slip velocity [e.g., *Nielsen et al.*, 2010]. We evaluate the influence of this parameter by varying the load point velocity (v_{lp}) relative to the background sliding velocity, v_0. By increasing v_{lp}, we also increase the eventual porosity to which the fault zone evolves in its new steady state, thereby increasing the effective time rate of dilatancy. With the increase in $d\phi/dt$ there is an increase in the rate of decompression of the pore fluid, yet the rate of fluid flow into the fault zone is controlled by the permeability of the fault zone. In general, we find that the higher v_{lp} the higher the magnitude of the dilatancy hardening. All parameters in these model runs are the same as above with the specification that $k = 10^{-19}$ m^2, $\varepsilon = 5 \times 10^{-4}$. We vary v_{lp} from a threefold increase over v_0, 10 to 30 μm/s, to a 100-fold increase from 10 μm/s to 1 mm/s.

[33] Using the Dieterich law, the relatively low value assumed for permeability results in a significant reduction in pore pressure at all values for v_{lp} (Figure 6a). When v_{lp} = 30 μm/s pore pressure is reduced by 2.1 MPa, scaling up to a 28.1 MPa reduction as a result of a jump to 1 mm/s. Using higher values for v_{lp} results in a higher magnitude of undrained pore pressure change (ΔP_{max}), independent of the increased potential for depressurization due to increased $d\varphi/dt$. The results of these runs show that the fault zone becomes increasingly undrained as v_{lp} is increased, with depressurization ranging from $0.23 \cdot \Delta P_{max}$ at 30 μm/s up to nearly $0.73 \cdot \Delta P_{max}$ at 1 mm/s.

[34] Shear strength increase resulting from the decompression of pore fluid in these cases is dramatic (Figure 6b). With only a 3X jump in velocity, the maximum shear strength is increased to 91.3 MPa, a response which completely overshadows the shear strength response due to the evolution of μ. When v_{lp} is stepped up to 1 mm/s the maximum shear strength of the fault zone reaches 106.5 MPa, dwarfing a purely drained response which would only lead to a peak shear strength of 90.7 MPa.

[35] Using Ruina state evolution results in in slightly more pore pressure reduction than Dieterich style evolution (Figure 6c). When v_{lp} = 30 μm/s, pore pressure is reduced by 2.3 MPa further reducing by 28.8 MPa at 1000 μm/s. ΔP_{max} is identical regardless of the type of state evolution used, resulting in a fault zone that depressurizes from 25% to 74% of ΔP_{max} using Ruina style state evolution. As with the Dieterich law, the fault zone becomes increasingly undrained at progressively higher shear rates.

[36] Shear strength is increased at all sliding velocities (Figure 6d). When v_{lp} = 30 μm/s the peak shear strength is 91.4 MPa, dwarfing the drained frictional response which would only lead to a peak of 90.14 MPa. At a load point velocity of 1 mm/s the shear strength increases to a maximum of 106.9 MPa, again completely overwhelming the purely frictional response.

3.4. Nondimensional Analysis

[37] It can be useful to evaluate numerical results in a nondimensional form. This approach is particularly helpful for understanding the extent of depressurization in a fluid saturated fault zone. We use the nondimensional terms

$$\left.\begin{aligned} u_D &= \frac{u}{D_C} \\ t_D &= \frac{tk}{\phi(\beta_W + \beta_\phi)\eta L^2} \\ \theta_D &= \frac{\theta v_0}{D_C} \\ P_D &= \frac{\Delta P_P}{P_{P0}} \quad or \quad P_D = \frac{\Delta P_P}{\Delta P_{max}} \end{aligned}\right\}, \tag{20}$$

where the subscript D denotes a dimensionless variable. P_D is presented in two formats, the first will provide a measurement of the degree of pore fluid depressurization

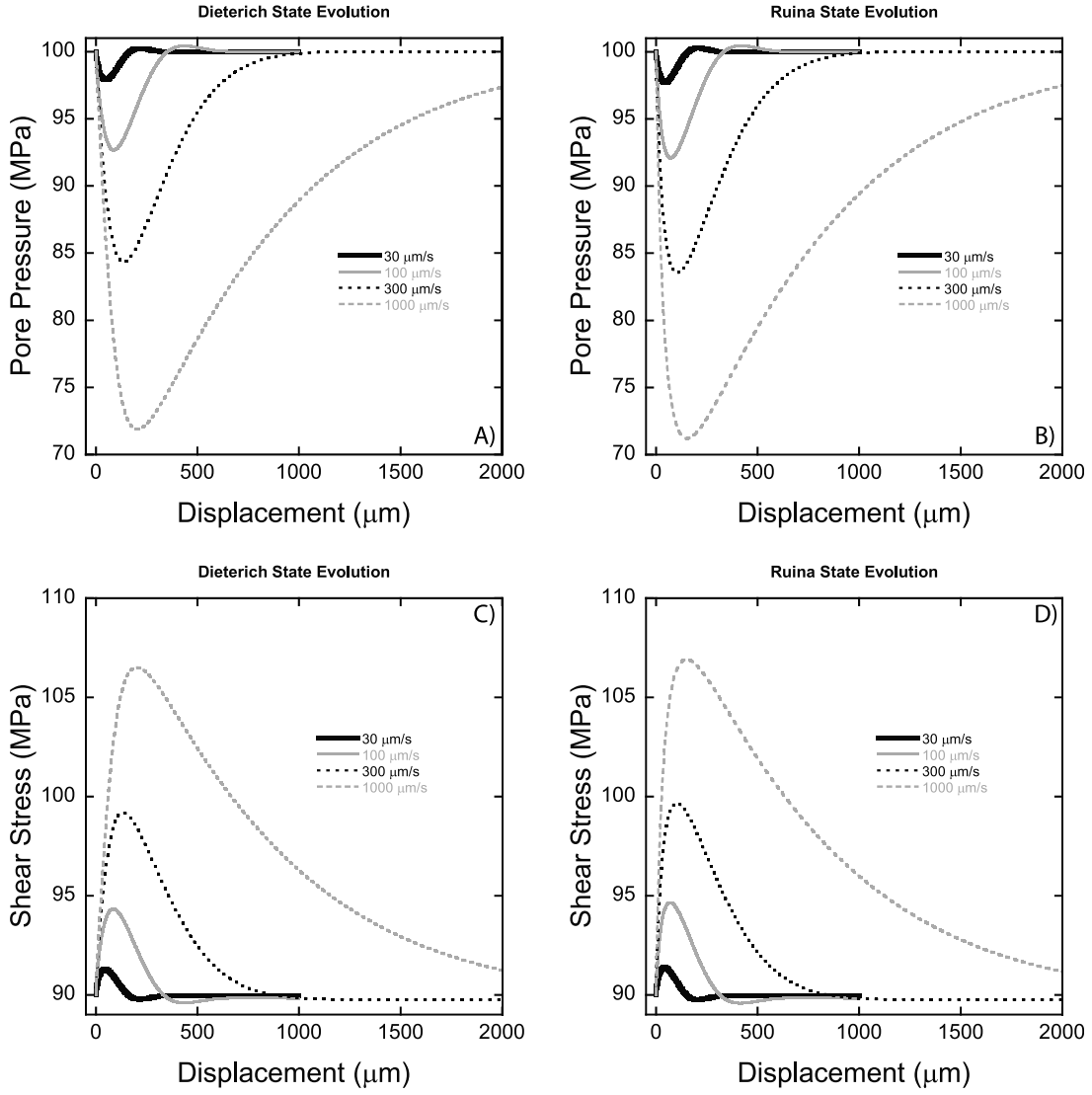

Figure 6. Effect of load point velocity (vlp) steps on (a, b) pore pressure and (c, d) shear strength evolution in a fault zone with a half-thickness of 3 mm. Figures 6a and 6c are for Dieterich style state evolution and Figures 6b and 6d are for Ruina state evolution. In all cases v_0 = 10 μm/s, a = 0.001, b = 0.0015, D_C = 25 μm, $\varepsilon = 5 \times 10^{-4}$, $k = 1 \times 10^{-19}$ m^2, σ_n = 250 MPa, P_0 = 100 MPa.

the fault zone experiences (Figures 7a, 7b, and 7c), and the second is a measure of how fully undrained the fault zone is as a result of dilational decompression (Figures 7d, 7e, and 7f). The transition from drained to undrained behavior for a stiff system ($K_s \rightarrow \infty$) is indexed by the dimensionless shear velocity $V_D = u_D/t_D = (L^2/k) \cdot (\nu\eta/K_W D_C)$ [*Samuelson et al.*, 2009], where $K_W = 1/\beta_W$. The first term represents the reciprocal rate of fluid loss by drainage, and the second term represents the rate of pore volume change by dilation or compaction. A threshold magnitude of $V_D \sim 1$ marks the transition from drained ($V_D \ll 1$) to undrained ($V_D \gg 1$) behavior. In the numerical experiments reported here L (3 mm), η (1.28×10^{-10} MPa·s), K_W (1456 MPa), and D_C (25 μm) are held constant so the transition from drained to undrained response scales with the ratio of shear velocity to permeability as $V_D = \frac{u_D}{t_D} \approx 3.13 \times 10^{-14}$ (meter seconds) $\cdot \frac{\nu}{k}$.

[38] Using Ruina style state evolution we follow the same basic pattern of analysis as that used in Figures 4c and 4d, Figures 5c and 5d, and Figures 6c and 6d, using the same parameter values as the analogous dimensional results. As permeability is reduced from 10^{-15} m^2 to 10^{-21} m^2 the gouge layer transitions from functionally drained to nearly completely undrained and ranges from 0 to ~8% total depressurization reaching $0.9*\Delta P_{\max}$ (Figures 7a and 7d). The transition appears to take place between $k = 10^{-17}$ m^2 and $k = 10^{-18}$ m^2, which corresponds to a change in V_D from ~0.09 to 0.9. Likewise, varying ε from 10^{-5} to 10^{-3} results in increasing total depressurization from less than 1% for small ε to 4% at large ε (Figure 7b). Interestingly, though, the degree of drainage of the gouge layer decreases from a depressurization of $0.35 \cdot \Delta P_{\max}$ at $\varepsilon = 10^{-5}$ to $0.21 \cdot \Delta P_{\max}$ at $\varepsilon = 10^{-3}$ (Figure 7e), suggesting that the gouge layer is more fully undrained at lower values of ε, a counterintuitive result. This appears to be the result of the high dilatancy

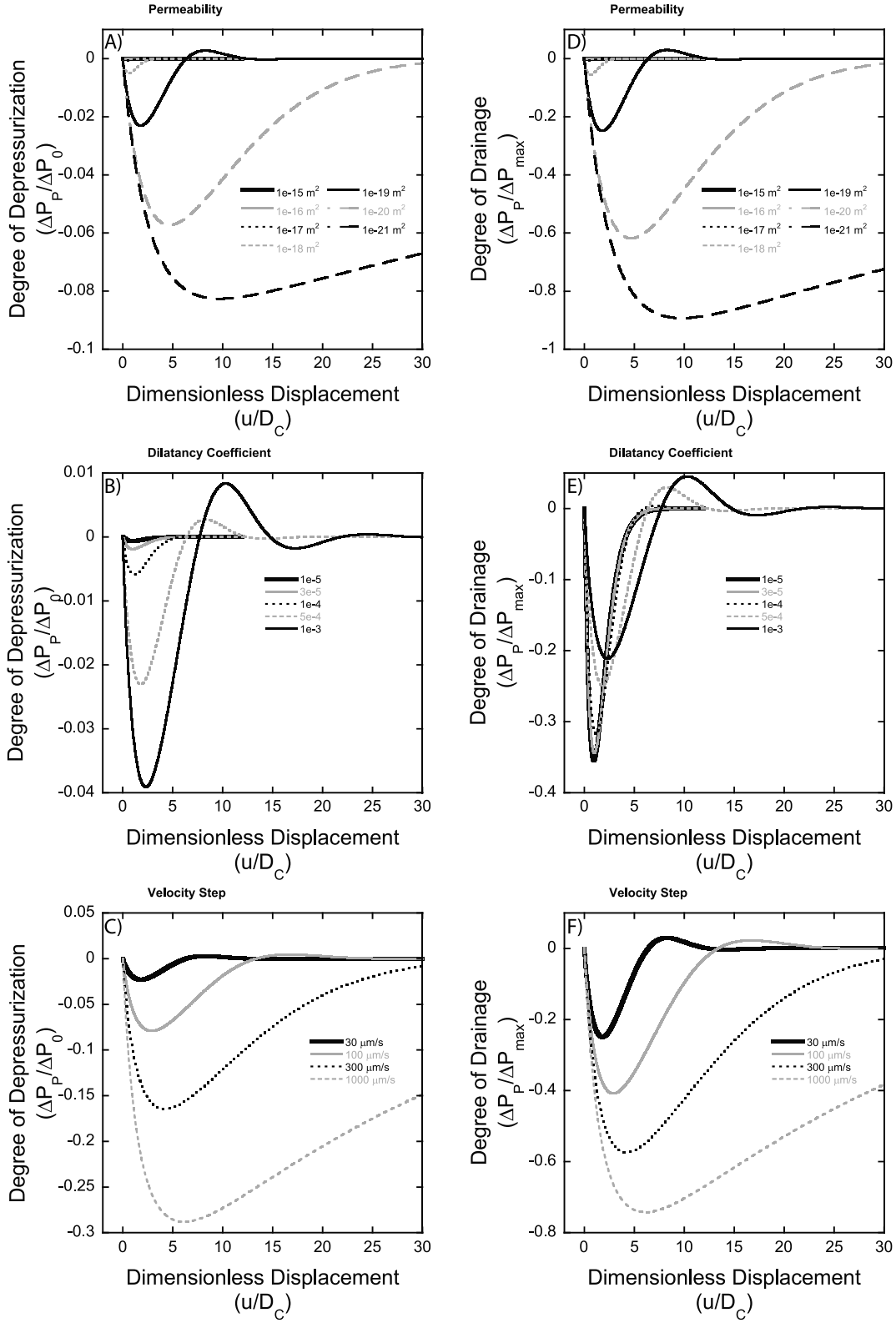

Figure 7. Dimensionless rate- and state-dependent pore pressure response to a velocity step using Ruina style state evolution. Shown on the left is pressure response normalized by the initial pore pressure (P_0), and shown on the right is pressure response normalized by the undrained pore pressure drop (ΔP_{max}). (a, d) Effect of permeability (k) from 10^{-15} to 10^{-21} m^2. (b, e) Effect of dilatancy coefficient (ε) from 10^{-5} to 10^{-3}. (c, f) Effect of load point velocity (v_{lp}) step size from 10 μm/s to 30, 100, 300, or 1000 μm/s. Except when the parameter is the relevant variable, $v_0 = 10$ μm/s, $a = 0.001$, $b = 0.0015$, $D_C = 25$ μm, $k = 1 \times 10$–19 m^2, $\varepsilon = 5 \times 10^{-4}$, $v_{lp} = 30$ μm/s, $\sigma_n = 250$ MPa, $P_0 = 100$ MPa.

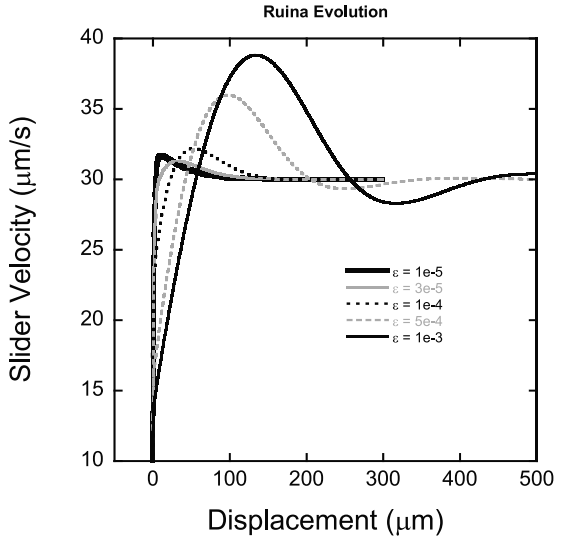

Figure 8. Showing the evolution of slider velocity as a result of an increase in load point velocity from 10 to 30 μm/s in a low permeability ($k = 1 \times 10^{-19}$ m^2) simulated fault zone with variable dilatancy coefficient (ε). As ε increases the decompression of the pore fluid is more pronounced, resulting in slowed acceleration of the slider toward 30 μm/s. This slowed acceleration allows more time for drainage resulting in the nonintuitive decreased total degree of depressurization seen in Figure 7e for higher values of ε. The increased harmonic ringing seen at higher values of ε appears to be a similar consequence of the inhibited acceleration which results in increasingly significant elastic overshoot of v_{lp}, causing the ringing.

coefficient leading to rapid decompression of the pore fluid and consequently slowed acceleration of the slider. During this slowed acceleration the dilatancy rate slows and the fault zone is able to drain enough to reduce the absolute efficacy of the pore fluid decompression (Figure 8). The slowed acceleration is evident in the offset of the pressure peaks to progressively larger shear displacements with increasing ε. In this case of variable ε, V_D is ~9.5, indicating a strongly undrained layer, it is important to note that V_D does not provide a complete description for the drainage state of the layer, as there is significant variability in depressurization based solely on a change in ε. This apparent inconsistency results from the effective magnitude of D_c increasing with an increase in ε (discussed later) and thus the effective magnitude of V_D is not constant for this suite (Figures 7b and 7e) despite k, L, v, η, and K_w all being invariant. This behavior is a consequence of the stiffness of the loading system, as this behavior is not manifest for an infinitely stiff system, where V_D is an adequate descriptor of drainage state [*Samuelson et al.*, 2009]. Finally, we see that increasing the size of the velocity step from 10 to 30 μm/s to 10–1000 μm/s results in an increase in total depressurization from approximately 2% to over 28% (Figure 7c) and that the degree of drainage in the layer ranges from $0.25 \cdot \Delta P_{\max}$ to $0.74 \cdot \Delta P_{\max}$ over the same velocity step range (Figure 7f).

[39] We chose to use Ruina style state evolution for this dimensionless analysis, noting that using Dieterich style evolution would result in differences of the same magnitude as the difference shown in Figures 4–6. The nondimensional analysis revealed that permeability (k), viscosity (η), and the square of the half-layer thickness (L^2) are linked in equations (18) and (20) as the ratio $\frac{k}{\eta L^2}$; therefore, though we achieve the results of Figure 4 and Figures 7a and 7d by decreasing the permeability of the gouge layer, the same response would be elicited by increasing the pore fluid viscosity or the layer half-thickness appropriately.

3.5. Effective Constitutive Parameters

[40] To determine the effective increase in the rate and state constitutive parameters, we took the model results of shear stress evolution from Figures 4 through 6 and determined least squares, best fit parameters assuming constant effective normal stress. The approach is identical to the process used to obtain friction constitutive parameters from laboratory data [e.g., *Blanpied et al.*, 1998]. We focus here on the effective direct effect a', related to the term a, from equation (3), and the effective critical slip distance, D_C', over which frictional strength evolves to the new background value. We model shear stress (τ) rather than friction (μ) because it is in the shear stress response to an increased sliding velocity that we can see the effect of transient depressurization of the fault zone, with massive increases in τ and D_C due to increased effective stress. We can describe the evolution of shear stress resulting from increased sliding velocity by multiplying equation (3) by the effective normal stress (σ'):

$$\tau = \tau_0 + A \ln\left(\frac{v}{v_0}\right) + B \ln\left(\frac{v_0 \theta}{D_C}\right), \tag{21}$$

where A and B are given by $a\sigma'$ and $b\sigma'$, respectively.

[41] We are interested in the potential role of pore fluid and dilational decompression in tectonic fault zones. Thus an inherent assumption in this approach is that σ' is constant throughout the evolution of shear stress. Although we know this is incorrect in detail for our models, this procedure provides effective values for A and D_C and highlights the potential role of dilatant hardening in complex fault behavior such as slow earthquakes and rupture nucleation. In all subsequent cases the drained values for A and D_C are 0.15 MPa and 25 μm, respectively.

[42] We varied the permeability of our fault zone over the range 10^{-15} to 10^{-21} m^2, and over that range, using both the Dieterich and Ruina state evolution equations, a gouge zone of thickness $2L$ (6 mm) ranges from being nearly completely drained to nearly completely undrained. As a result of this transition, we move from a situation where $A' \approx A$ and $D_C' \approx D_C$ when the layer is drained to a situation where $A' \gg A$ and $D_C' \gg D_C$ (Figure 9). When $k \geq 10^{-16}$ m^2 the Dieterich law shows no change in A' from the input value, D_C' is likewise unaffected by what small pore fluid depressurization takes place at these permeabilities. At lower permeabilities ($k < 10^{-16}$ m^2) A' and D_C' progressively increase. When $k = 10^{-17}$ m^2 the effectiveness of dilatancy hardening at increasing A' and D_C' is small but noticeable with $A' =$ 0.17 MPa and $D_C' = 31.5$ μm. At $k = 10^{-21}$ m^2 A' experiences an over 30-fold increase to 4.6 MPa and D_C' has increased over 60 times to 1616 μm.

[43] Ruina state evolution results in similar, but subtly different, changes in D_C' and A' as permeability of the fault

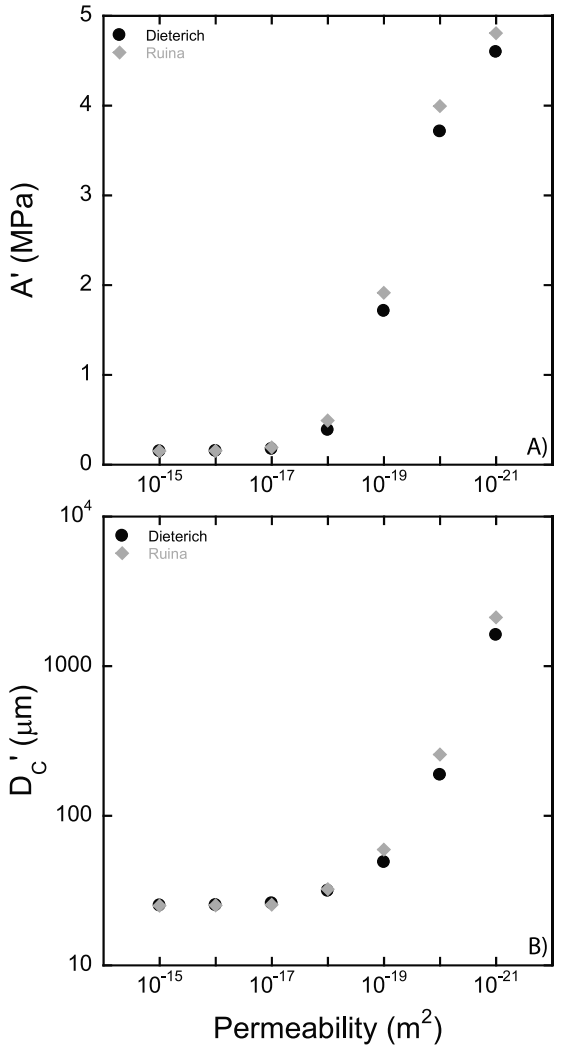

Figure 9. Effective alteration of the friction constitutive parameters A and D_C as a function of decreasing gouge layer permeability. Parameters are determined by inverse fitting of data from Figures 4b and 4d. (a) The parameter A' is the effective value of the direct effect, which controls the increase in shear strength in response to a velocity step. (b) D_C' is the effective value of the critical slip distance, the sliding distance over which friction evolves from one steady state to another in response to a velocity step.

zone changes. At relatively high permeability ($k \geq 10^{-16}$ m^2) the fault zone does not experience any significant dilatant hardening resulting in increased maximum shear strength or critical slip distance. When permeability is less than 10^{-16} m^2 both A' and D_C' are increased over the input value. At $k = 10^{-17}$ m^2 A' is increased to 0.19 MPa, and D_C' is increased, though only very slightly, to 25.4 μm. When $k = 10^{-21}$ m^2 the increases in A' and D_C' are dramatic with $A' = 4.9$ MPa and $D_C' = 2116$ μm. Even though a visual comparison of Figures 4a and 4c shows very similar evolution of shear strength, D_C' is significantly larger using Ruina evolution because of the inherently rapid evolution of that law. The evolution of shear strength using Ruina at low permeability is very similar to that using Dieterich because of the large reduction in pore pressure and the subsequent flow of fluid into the fault zone which is time dependent, so while the shear stress lines themselves look very similar, in order to fit the same evolution using the Ruina law requires a much larger D_C' than when using Dieterich evolution.

[44] Figure 10 shows the results of inverting the model data when we vary the dilatancy coefficient (ε) over the experimentally determined range 10^{-5} to 10^{-3}. We used a relatively low permeability, $k = 10^{-19}$ m^2, and found that fault zone pore fluid was depressurized at all values of ε, significantly so beginning at $\varepsilon \geq 10^{-4}$. At $\varepsilon = 10^{-5}$ D_C' is increased to 32 μm using the Dieterich law and 35 μm using Ruina. The direct effect is effectively increased to 0.16 in both Dieterich and Ruina state evolution schemes. As ε increases, the magnitude of dilatancy hardening increases, and with it A' and D_C' are likewise increased. When $\varepsilon = 10^{-3}$ dilatancy hardening is significant resulting in $A' = 3.2$ MPa and $D_C' = 53$ μm using Dieterich evolution and $A' = 3.5$ MPa

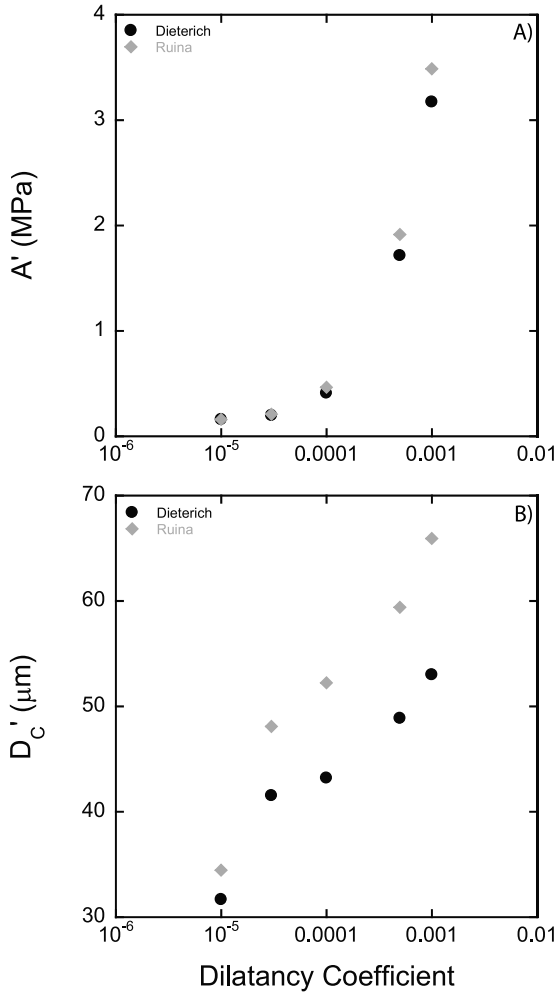

Figure 10. Effective alteration of the friction constitutive parameters A and D_C as a function of variable dilatancy coefficient. Parameters are determined by inverse fitting of data from Figure 5b and 5d. (a) A' is the effective value of the direct effect, which controls the increase in shear strength in response to a velocity step. (b) D_C' is the effective value of the critical slip distance, the sliding distance over which friction evolves from one steady state to another in response to a velocity step.

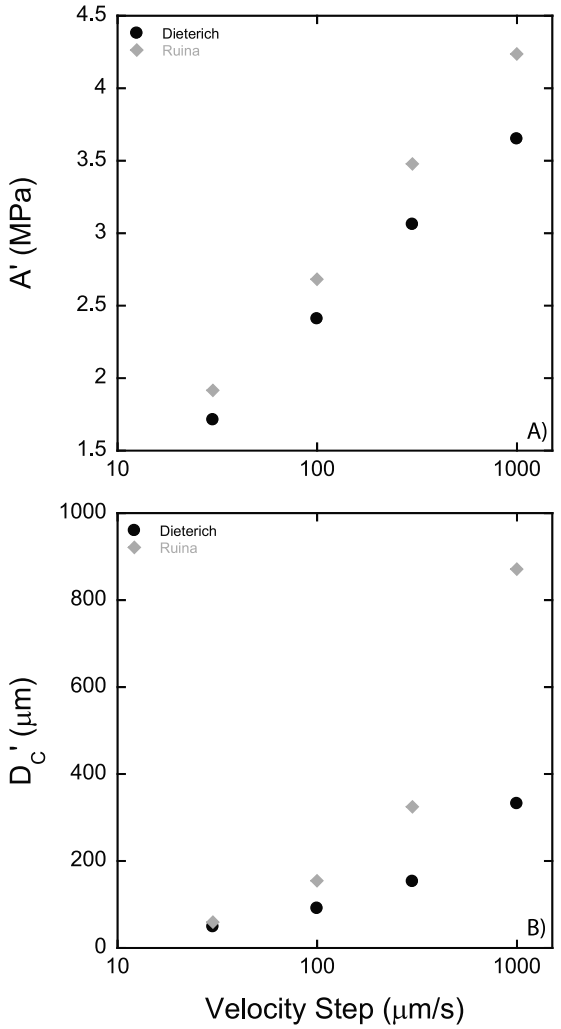

Figure 11. Effective alteration of the constitutive parameters A and D_C as a function of increasing load-point velocity. Parameters are determined by inverse fitting of data from Figure 6b and 6d. (a) A' is the effective value of the direct effect, which controls the increase in shear strength in response to a velocity step. (b) D_C' is the effective value of the critical slip distance, the sliding distance over which friction evolves from one steady state to another in response to a velocity step.

and D_C' = 66 μm using Ruina evolution. Again that D_C' is larger using the Ruina law is consistent with the time-dependent flow of fluid into the fault zone and the general behavior of the Ruina law.

[45] Finally, we varied the magnitude of the increase in shearing velocity (v_{lp}) of the fault zone, in all cases the initial shear velocity is 10 μm/s, we then increase the velocity to 30, 100, 300, or 1000 μm/s. We used k = 10^{-19} m^2 and $\varepsilon = 5 \times 10^{-4}$ for all simulations, and found significant dilatancy hardening all v_{lp}. At v_{lp} = 30 μm/s A' equals 1.7 and 1.9 MPa for the Dieterich and Ruina laws, respectively; both cases are well above the drained value of 0.15 MPa. D_C' at v_{lp} = 30 μm/s is also above the input value, 49 μm for Dieterich evolution and 59 μm for Ruina evolution (Figure 11). At v_{lp} = 1000 μm/s A' is 3.6 MPa for Dieterich and 4.2 MPa for Ruina. D_C' is larger for Ruina at all velocity steps for reasons we have previously described, growing to 871 μm at v_{lp} = 1000 μm/s and only 332 μm using Dieterich evolution. Again it is the time dependency of the decay of shear strength that leads to the extremely large values for D_C' for Ruina evolution, even as compared to Dieterich evolution.

3.6. Phase Plane Analysis

[46] We present a phase plane analysis of the data in sections 3.1 to 3.3 (Figures 12–14); such plots are particularly useful in illustrating the progression of shear stress as the shearing velocity accelerates from v_0 to v_{lp}. For variable

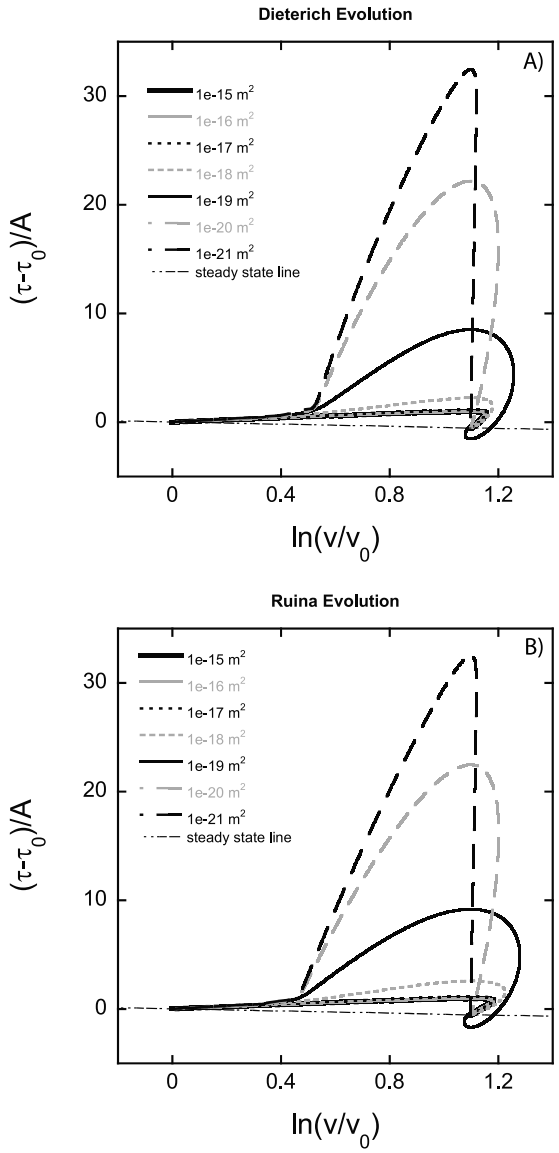

Figure 12. Phase plane analysis of the data from Figures 4b and 4d. Increase in shear strength (normalized by the direct effect) is plotted as a function of the slider velocity as it accelerates from v_0 to v_{lp}. Steady state line indicates the steady state shear strength for velocity steps of any given size for the case (a-b) = −0.0005. (a) Dieterich style state evolution over the permeability range 10^{-15}–10^{-21} m^2. (b) Ruina style state evolution.

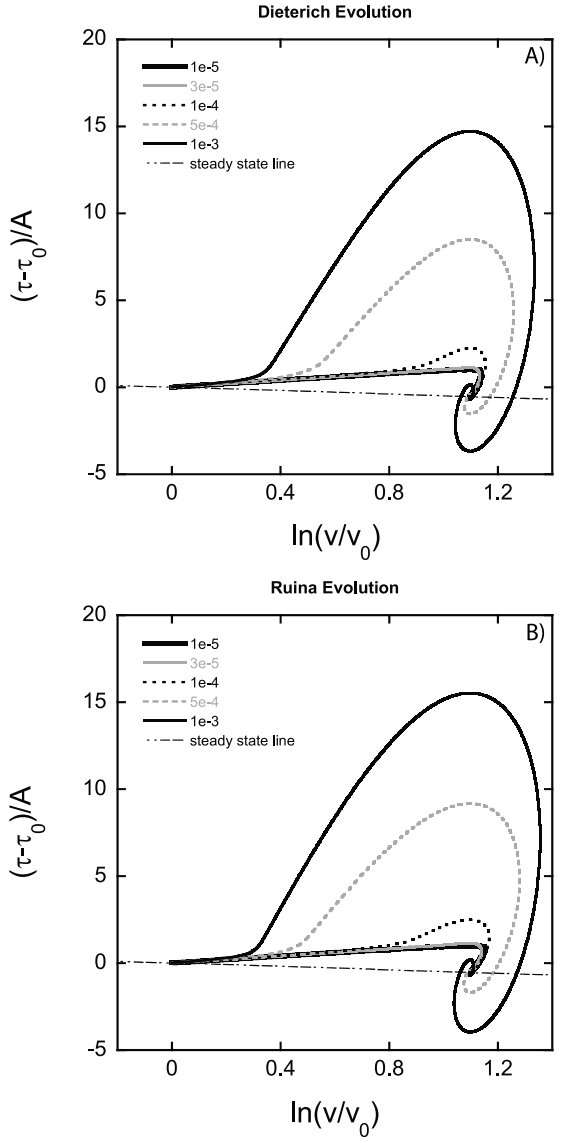

Figure 13. Phase plane analysis of the data from Figures 5b and 5d. Steady state line indicates the steady state shear strength for velocity steps of any given size for the case $(a\text{-}b) = -0.0005$. (a) Dieterich style state evolution over the dilatancy coefficient range 10^{-5}–10^{-3}. (b) Ruina style state evolution.

permeability and dilatancy coefficient the phase plane plots provide further indication of how similar the shear strength evolution is for the two state evolution schemes (Figures 12 and 13), whereas Figure 14 shows that there is a fairly significant difference between the schemes when comparing the evolution of shear strength for velocity steps of differing size. In Figures 12–14 the results using Dieterich state evolution are shown at the top and Ruina evolution is shown at the bottom. The thin dashed line represents the steady state reduction in shear strength that results from the velocity weakening parameters we chose: $(a\text{-}b) = -0.0005$. For a threefold increase in sliding velocity when $\varepsilon = 5 \times 10^{-4}$, shear stress evolution behaves in a nearly completely drained manner when permeability is at least 10^{-17} m^2 for both styles of state evolution. At permeabilities lower than 10^{-17} m^2 the shear stress is increased over a drained layer, and it appears that the layer begins to be depressurized when $\ln(v/v_0) \approx 0.5$ or in this specific case when the velocity has reached about 16 μm/s, on the way toward 30 μm/s (Figure 12). Comparison of Dieterich and Ruina style state evolution over a dilatancy coefficient range from 10^{-5} to 10^{-3} indicates that the differences based solely on style of state evolution are small, beyond simply the increased magnitude of dilatancy hardening experienced under the Ruina law (Figure 13). We use $v_{lp} = 30$ μm/s in all cases when varying the dilatancy coefficient, and $k = 10^{-19}$ m^2. As the shear velocity of the fault zone accelerates from v_0 to v_{lp}, the velocity at which significant dilatancy hardening begins is decreased at higher values for ε. When $\varepsilon \leq 3 \times 10^{-5}$ there is no obvious change

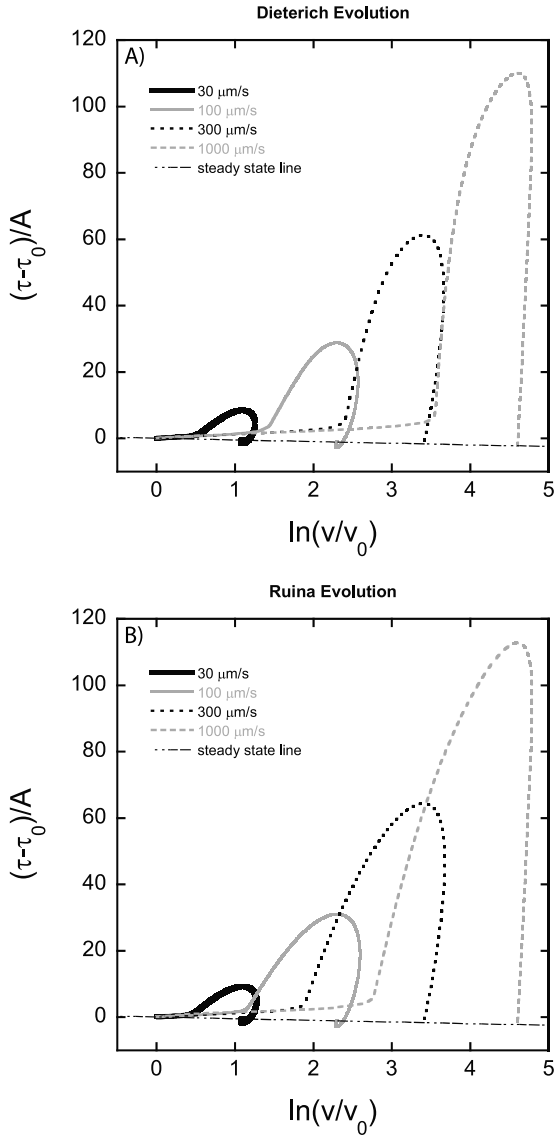

Figure 14. Phase plane analysis of the data from Figures 6b and 6d. Steady state line indicates the steady state shear strength for velocity steps of any given size for the case $(a\text{-}b) = -0.0005$. (a) Dieterich style state evolution for velocity steps from 10 μm/s to 30, 100, 300, or 1000 μm/s. (b) Ruina style state evolution.

from a layer that behaves in a drained manner, but beginning at $\varepsilon = 10^{-4}$ the velocity at which the fault zone begins to depressurize decreases from ~22 μm/s to ~13 μm/s at $\varepsilon = 10^{-3}$.

[47] Increasing the size of the step in load-point velocity results in interesting differences between the Dieterich and Ruina styles of state evolution (Figure 14). The thin dashed line shows the steady state decrease that is expected in shear strength as a result of any given size of velocity increase and is again indicative of the velocity weakening nature of the model we have created. These plots are of particular interest because they show a subtle difference between the two styles of state evolution. For any given increase in load point velocity depressurization of the layer begins at a lower velocity for Ruina state evolution than for Dieterich evolution. *Bayart et al.* [2006] indicate that for large velocity steps ($v_{lp} \approx 100 v_0$) the Ruina formulation of state evolution provides a much more accurate representation of the response of friction to velocity steps, and in a similar way the results presented here in Figure 14, could allow for the tuning of a physical experiment that may shed light on the superiority of one state evolution formulation over the other.

4. Discussion

[48] In order for a fault zone to be capable of hosting unstable stick-slip sliding, two conditions must be met. First is that upon an increase in shearing velocity the new steady state shear strength of the fault zone must be lower than prior to the increase, i.e., $d\tau_{ss}/dv < 0$ [*Dieterich*, 1978, 1979; *Ruina*, 1983]. In cases where $d\tau_{ss}/dv > 0$ a fault zone will slide stably. The first instability condition $d\tau_{ss}/dv < 0$ is met in all cases in the numerical results presented here because we dictated that $(a\text{-}b) < 0$. As long as a fault zone is not completely undrained, dilatancy hardening only delays the onset of velocity weakening in a fault zone, it does not change velocity weakening into velocity strengthening.

[49] The second condition is based upon the elastic stiffness of the loading system. Unstable frictional slip requires that the stiffness of the loading system (K_s) be lower than a threshold value K_{cr} given by the constitutive response. In the case of our simulations K_s is far higher than K_{cr} for all simulations, but when $K_s < K_{cr}$, the shear strength of the fault zone is able to drop faster than the applied elastic load. During the period when the load provided by the spring is greater than the shear strength of the fault zone, the slider will accelerate until such time as the loading system and the frictional strength have balanced one another and the slider comes to a stop or at least returns to its preinstability shearing velocity. K_{cr} is therefore controlled by the distance over which shear stress evolves from one steady state to another upon an increase in shearing velocity and also on the need to overcome the peak shear strength after the onset of the faster shearing velocity:

$$K_{cr} = \frac{\sigma'(b-a)}{D_C}\left[1 + \frac{mv_0^2}{\sigma' a D_C}\right] = \frac{B-A}{D_C} + \frac{(B-A)mv_0^2}{AD_C^2}, \quad (22)$$

where m is the mass of the slider. This formulation of the critical stiffness (K_{cr}) takes into account inertial effects, which can be removed by allowing $m = 0$, simplifying equation (22) to the formulation presented by *Segall and Rice* [1995] $K_{cr} = \sigma' \left(\frac{b-a}{D_c}\right)$, though doing so would negate the contribution of a high peak shear strength [e.g., *Roy and Marone*, 1996] to the effective alteration of K_{cr}. Our numerical model shows that, as a result of quasi-undrained dilatancy, the effective rate and state parameters A' and D_C' are increased beyond what they would be in a fully drained fault zone. Even at a relatively slow slip velocity of 30 μm/s, D_C' is effectively increased 80 times, from 25 μm to 2.1 mm (using Ruina evolution), and A' from 0.15 to 4.8 MPa in a very low permeability fault zone. As a result of these increases, the critical stiffness of the loading system becomes much smaller as both A' and D_C' are in the denominator of equation (22). As the critical slip distance becomes increasingly large in a nearly undrained fault zone, the inertial portion of equation (22) is of vanishing importance as D_C is squared in the denominator. In the most extreme case presented here ($k = 10^{-21}$ m^2) the inertial term of equation (22) is nearly 200,000 times smaller than in a completely drained fault zone, solely due to the effective increase in A' and D_C'. Even ignoring the inertial term, our numerical results suggest the need for a loading system that is 80 times more compliant than in a drained fault zone because of the increase in D_C'. Previous analyses [*Rudnicki and Chen*, 1988; *Segall and Rice*, 1995; *Garagash and Rudnicki*, 2003a, 2003b] indicate that pore fluid depressurization driven by fault zone dilatancy favors stable sliding over unstable stick-slip. The analysis presented here infers that nucleating dynamic earthquake slip within a region where dilatancy hardening is efficient would prove difficult at least in part due to effective increases in the rate and state friction constitutive parameters and associated alteration of the effective critical stiffness (K_{cr}'). Arguments have been made that seismicity varies with depth due to changes in the combined rate and state friction parameter $(a\text{-}b)$ which can vary with depth from $(a\text{-}b) > 0$ at shallow depths where fault wear material is unlithified, grading to $(a\text{-}b) < 0$ at seismogenic depths where there is increased lithification of the fault gouge, and finally where $(a\text{-}b)$ is once again greater than zero at extreme depths where crystal plasticity promotes stable sliding [*Scholz*, 1998; *Saffer and Marone*, 2003]. There could likewise be changes in the drainage state of fault zone with depth or lateral extent, leading to areas where dilatancy hardening is so efficient that earthquakes simply cannot nucleate leading to a stably creeping fault. Additionally, such regions of efficient dilatancy hardening would tend to arrest the propagation of shear rupture, similar to those regions described as conditionally stable by *Scholz* [1998]. This type of spatial complexity in fault zone drainage state was shown to result in realistic spatiotemporal complexity in earthquake nucleation in the numerical analyses of *Hillers et al.* [2006] and *Hillers and Miller* [2006, 2007] on simulated dilatant fault zones with spatial variations in fault constitutive parameters and was in part attributed to large values of D_C, which we have shown can be effectively produced by efficient dilatant hardening, leading to increases of several orders of magnitude.

[50] For simulations involving variable permeability and velocity step size (Figures 4 and 5) the periodic ringing that is evident (particularly when $k = 10^{-19}$ m^2 and $v_{lp} = 30$ μm/s) is damped as the permeability is further decreased or the velocity step size is increased. This is largely due to the fact that the shear stress evolution is only partially elastic, and

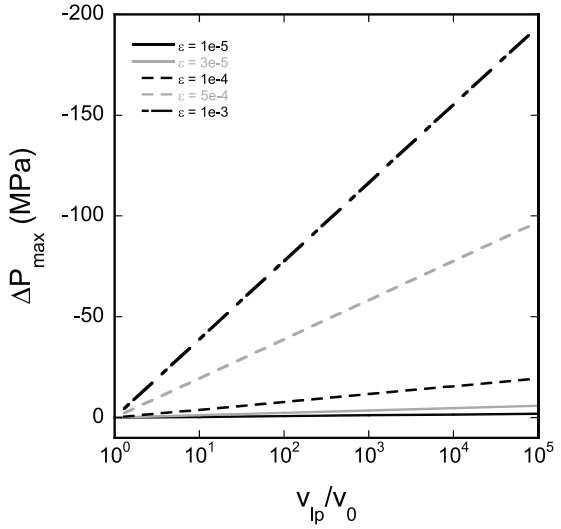

Figure 15. Undrained pore pressure drop (ΔP_{max}) as a function of velocity step size for the dilatancy coefficient range used and $\varphi_0 = 0.05$. As ε and (v_{lp}/v_0) increase, volumetric strain and therefore the potential for pore fluid decompression likewise increase.

once the drainage of the layer becomes the dominant mechanism of shear stress evolution such elastic ringing is damped. However, in the case of variable dilatancy coefficient, the ringing becomes more pronounced as ε is increased, the enhancement seems to be a result of the coupling of velocity evolution and the dilatancy coefficient in determining the porosity of the fault zone. As the slider accelerates, it elastically overshoots the load-point velocity, causing strong decompression of the pore fluid; consequently, as the slider decelerates back toward v_{lp}, the pore fluid is compressed further, slowing the slider to a value less than v_{lp}. This process is exacerbated by large values for ε because of the direct coupling between the dilatancy coefficient and the magnitude of porosity change (Figure 8).

[51] The increases in A' and D_C' are shown here to be so large that it becomes difficult to imagine earthquakes nucleating in any fault zone, particularly considering that our velocity steps were from 10 to 30 μm/s in most cases. At $k = 10^{-21}$ m^2 the fault zone is depressurized to nearly 90% of ΔP_{max} as a result of a threefold increase in shearing velocity. As v_{lp} reaches seismic rates (~1 m/s $\rightarrow$ $v_{lp}/v_0 = 10^5$), ΔP_{max} becomes so large (Figure 15) that a completely depressurized fault zone is reasonable, leading to an effective increase in both A and D_C so large that nucleation of instabilities is nearly impossible to imagine. Since earthquakes do occur, however, there must be some other way of dissipating shear stress rapidly enough to result in a critical stiffness that could allow stick-slip unstable sliding, perhaps through thermal pressurization of the pore fluid [*Bizzarri and Cocco*, 2006a, 2006b; *Rice*, 2006; *Segall and Rice*, 2006], enhanced along-strike permeability, or possibly through a transient change in the location of the slip surface from the center to the edge of the fault core as decreased fluid pressure strengthens the innermost regions of the fault core.

[52] Finally, it is worth noting that our simulations may provide some reasoning behind the discrepancy between laboratory and field estimates of the critical slip distance. Experimental studies of D_C are typically in the range of 1–200 μm [*Marone et al.*, 1990; *Mair and Marone*, 1999], whereas *Scholz* [1988b] suggested the critical slip distance of natural faults to be approximately 10^{-3} to 10^{-2} m based on estimates of fault roughness. Our results show that under very poorly drained conditions ($k < 10^{-19}$ m^2) the critical slip distance in an experimental fault zone could effectively approach the values suggested by field observations.

5. Conclusions

[53] Our work builds on previous studies involving complex simulations of the stability of dilatant fault zones. We provide a detailed analysis of the effective rate and state friction parameters A and D_C as a function of changes in the drainage state of a simulated experimental fault zone enforced by changes in fault zone permeability (k), dilatancy coefficient (ε), and step increases in shearing velocity (v_{lp}). We find in all cases that reducing k or increasing ε or v_{lp} leads to a progressively more poorly drained fault zone resulting in effective increases in the rate and state parameters A and D_C via the process of dilatancy hardening. The increase in these constitutive parameters has the effect of reducing the critical stiffness of fault zones to the point that nucleation of earthquakes in, or the propagation of earthquakes through, poorly drained regions of faults is severely inhibited. Our work shows that mechanisms other than effective stress changes may be needed to reduce fault strength during earthquake nucleation.

[54] **Acknowledgments.** We gratefully acknowledge support from the National Science Foundation under grant numbers OCE-0648331, ANT-0538195, EAR-0510182, and EAR-0911569. This paper was significantly improved based on the thoughtful comments of two anonymous reviewers.

References

Andrews, D. J. (2002), A fault constitutive relation for thermal pressurization of pore fluid, *J. Geophys. Res.*, *107*(B12), 2363, doi:10.1029/2002JB001942.

Barbot, S., Y. Fialko, and D. Sandwell (2008), Effect of a compliant fault zone on the inferred earthquake slip distribution, *J. Geophys. Res.*, *113*, B06404, doi:10.1029/2007JB005256.

Bayart, E., A. M. Rubin, and C. J. Marone (2006), Evolution of fault friction following large velocity jumps, *Eos Trans. AGU*, *87*(52), Fall Meet. Suppl., Abstract S31A–0180.

Bizzarri, A. (2009), What does control earthquake ruptures and dynamic faulting? A review of different competing mechanisms, *Pure Appl. Geophys.*, *166*, 741–776, doi:10.1007/s00024-009-0494-1.

Bizzarri, A., and M. Cocco (2006a), A thermal pressurization model for the spontaneous dynamic rupture propagation on a three-dimensional fault: 1. Methodological approach, *J. Geophys. Res.*, *111*, B05303, doi:10.1029/2005JB003862.

Bizzarri, A., and M. Cocco (2006b), A thermal pressurization model for the spontaneous dynamic rupture propagation on a three-dimensional fault: 2. Traction evolution and dynamic parameters, *J. Geophys. Res.*, *111*, B05304, doi:10.1029/2005JB003864.

Blanpied, M. L., C. J. Marone, D. A. Lockner, J. D. Byerlee, and D. P. King (1998), Quantitative measure of the variation in fault rheology due to fluid-rock interactions, *J. Geophys. Res.*, *103*(B5), 9691–9712, doi:10.1029/98JB00162.

Brantut, N., A. Schubnel, J.-N. Rouzaud, F. Brunet, and T. Shimamoto (2008), High-velocity frictional properties of a clay-bearing fault gouge and implications for earthquake mechanics, *J. Geophys. Res.*, *113*, B10401, doi:10.1029/2007JB005551.

Brantut, N., A. Schubnel, J. Corvisier, and J. Sarout (2010), Thermochemical pressurization of faults during coseismic slip, *J. Geophys. Res.*, *115*, B05314, doi:10.1029/2009JB006533.

Byerlee, J. (1978), Friction of rocks, *Pure Appl. Geophys.*, *116*, 615–626, doi:10.1007/BF00876528.

Dieterich, J. H. (1978), Time-dependent friction and the mechanics of stick-slip, *Pure Appl. Geophys.*, *116*, 790–806, doi:10.1007/BF00876539.

Dieterich, J. H. (1979), Modeling of rock friction 1. Experimental results and constitutive equations, *J. Geophys. Res.*, *84*(B5), 2161–2168, doi:10.1029/JB084iB05p02161.

Dieterich, J. H. (1981), Constitutive properties of faults with simulated gouge, in *Mechanical Behavior of Crustal Rocks: The Handin Volume*, *Geophys. Monogr. Ser.*, vol. 24, edited by N. L. Carter et al., pp. 103–120, AGU, Washington, D.C.

Faoro, I., A. Niemeijer, C. Marone, and D. Elsworth (2009), Influence of shear and deviatoric stress on the evolution of permeability in fractured rock, *J. Geophys. Res.*, *114*, B01201, doi:10.1029/2007JB005372.

Frye, K. M., and C. Marone (2002), Effect of humidity on granular friction at room temperature, *J. Geophys. Res.*, *107*(B11), 2309, doi:10.1029/2001JB000654.

Garagash, D. I., and J. W. Rudnicki (2003a), Shear heating on a fluid-saturated slip-weakening dilatant fault zone 1. Limiting regimes, *J. Geophys. Res.*, *108*(B2), 2121, doi:10.1029/2001JB001653.

Garagash, D. I., and J. W. Rudnicki (2003b), Shear heating on a fluid-saturated slip-weakening dilatants fault zone: 2. Quasi-drained regime, *J. Geophys. Res.*, *108*(B10), 2472, doi:10.1029/2002JB002218.

Harvey, A. H., and D. G. Friend (2004), Physical properties of water, in *Aqueous Systems at Elevated Temperatures and Pressures: Physical Chemistry in Water, Steam, and Hydrothermal Solutions*, edited by D. A. Palmer et al., pp. 1–27, Elsevier, London, doi:10.1016/B978-012544461-3/50002-8.

Hillers, G., and S. A. Miller (2006), Stability regimes of a dilatant, fluid-infiltrated fault plane in a three dimensional elastic solid, *J. Geophys. Res.*, *111*, B08304, doi:10.1029/2005JB003872.

Hillers, G., and S. A. Miller (2007), Dilatancy controlled spatiotemporal slip evolution of a sealed fault with spatial variations of the pore pressure, *Geophys. J. Int.*, *168*, 431–445, doi:10.1111/j.1365-246X.2006.03167.x.

Hillers, G., Y. Ben-Zion, and P. M. Mai (2006), Seismicity on a fault controlled by rate- and state-dependent friction with spatial variations of the critical slip distance, *J. Geophys. Res.*, *111*, B01403, doi:10.1029/2005JB003859.

Hubbert, M. K., and W. W. Rubey (1959), Role of fluid pressure in mechanics of overthrust faulting: 1. Mechanics of fluid-filled porous solids and its application to overthrust faulting, *Geol. Soc. Am. Bull.*, *70*(2), 115–166.

Ikari, M. J., D. M. Saffer, and C. Marone (2009), Frictional and hydrologic properties of clay-rich fault gouge, *J. Geophys. Res.*, *114*, B05409, doi:10.1029/2008JB006089.

Liu, Y., and A. M. Rubin (2010), Role of gouge dilatancy on aseismic deformation transients, *J. Geophys. Res.*, *115*, B10414, doi:10.1029/2010JB007522.

Mair, K., and C. Marone (1999), Friction of simulated fault gouge for a wide range of velocities and normal stresses, *J. Geophys. Res.*, *104*(B12), 28,899–28,914, doi:10.1029/1999JB900279.

Marone, C. (1998), Laboratory-derived friction laws and their application to seismic faulting, *Annu. Rev. Earth Planet. Sci.*, *26*, 643–696, doi:10.1146/annurev.earth.26.1.643.

Marone, C., C. Raleigh, and C. Scholz (1990), Frictional behavior and constitutive modeling of simulated fault gouge, *J. Geophys. Res.*, *95*(B5), 7007–7025, doi:10.1029/JB095iB05p07007.

Mitchell, T. M., and D. R. Faulkner (2008), Experimental measurements of permeability evolution during triaxial compression of initially intact crystalline rocks and implications for fluid flow in fault zones, *J. Geophys. Res.*, *113*, B11412, doi:10.1029/2008JB005588.

Nielsen, S., J. Taddeucci, and S. Vinciguerra (2010), Experimental observation of stick-slip instability fronts, *Geophys. J. Int.*, *180*(2), 697–702, doi:10.1111/j.1365-246X.2009.04444.x.

Rice, J. R. (2006), Heating and weakening of faults during earthquake slip, *J. Geophys. Res.*, *111*, B05311, doi:10.1029/2005JB004006.

Rice, J. R., and J. W. Rudnicki (1979), Earthquake precursory effects due to pore fluid stabilization of a weakening fault zone, *J. Geophys. Res.*, *84*(B5), 2177–2193, doi:10.1029/JB084iB05p02177.

Roy, M., and C. Marone (1996), Earthquake nucleation on model faults with rate- and state-dependent friction: Effects of inertia, *J. Geophys. Res.*, *101*(B6), 13,919–13,932, doi:10.1029/96JB00529.

Rubin, A. M. (2008), Episodic slow slip events and rate-and-state friction, *J. Geophys. Res.*, *113*, B11414, doi:10.1029/2008JB005642.

Rubin, A. M. (2011), Designer friction laws for bimodal slow slip propagation speeds, *Geochem. Geophys. Geosyst.*, *12*, Q04007, doi:10.1029/2010GC003386.

Rudnicki, J. W., and C. Chen (1988), Stabilization of a rapid frictional slip on a weakening fault by dilatant hardening, *J. Geophys. Res.*, *93*(B5), 4745–4757, doi:10.1029/JB093iB05p04745.

Ruina, A. (1983), Slip instability and state variable friction laws, *J. Geophys. Res.*, *88*(B12), 10,359–10,370, doi:10.1029/JB088iB12p10359.

Saffer, D. M., and C. Marone (2003), Comparison of smectite- and illite-rich gouge frictional properties: Application to the updip limit of the seismogenic zone along subduction megathrusts, *Earth Planet. Sci. Lett.*, *215*, 219–235, doi:10.1016/S0012-821X(03)00424-2.

Samuelson, J., D. Elsworth, and C. Marone (2009), Shear-induced dilatancy of fluid-saturated faults: Experiment and theory, *J. Geophys. Res.*, *114*, B12404, doi:10.1029/2008JB006273.

Scholz, C. (1988a), Mechanisms of seismic quiescences, *Pure Appl. Geophys.*, *126*(2–4), 701–718, doi:10.1007/BF00879016.

Scholz, C. (1988b), The critical slip distance for seismic faulting, *Nature*, *336*, 761–763, doi:10.1038/336761a0.

Scholz, C. (1998), Earthquakes and friction laws, *Nature*, *391*, 37–42, doi:10.1038/34097.

Segall, P., and J. Rice (1995), Dilatancy, compaction, and slip instability of a fluid-infiltrated fault, *J. Geophys. Res.*, *100*(B11), 22,155–22,171, doi:10.1029/95JB02403.

Segall, P., and J. Rice (2006), Does shear heating of pore fluid contribute to earthquake nucleation? *J. Geophys. Res.*, *111*, B09316, doi:10.1029/2005JB004129.

Segall, P., A. M. Rubin, A. M. Bradley, and J. R. Rice (2010), Dilatant strengthening as a mechanism for slow slip events, *J. Geophys. Res.*, *115*, B12305, doi:10.1029/2010JB007449.

Sleep, N. (1995), Frictional heating and the stability of rate and state dependent friction, *Geophys. Res. Lett.*, *22*(20), 2785–2788, doi:10.1029/95GL02801.

Sleep, N. H. (2006), Frictional dilatancy, *Geochem. Geophys. Geosyst.*, *7*, Q10008, doi:10.1029/2006GC001374.

Tanikawa, W., M. Sakaguchi, O. Tadai, and T. Hirose (2010), Influence of fault slip rate on shear-induced permeability, *J. Geophys. Res.*, *115*, B07412, doi:10.1029/2009JB007013.

Ujiie, K., and A. Tsutsumi (2010), High-velocity frictional properties of clay-rich fault gouge in a megasplay fault zone, Nankai subduction zone, *Geophys. Res. Lett.*, *37*, L24310, doi:10.1029/2010GL046002.

Wagner, W., and A. Pruss (2002), The IAPWS formulation 1995 for the thermodynamic properties of ordinary water substance for general and scientific use, *J. Phys. Chem. Ref. Data*, *31*, 387–535, doi:10.1063/1.1461829.

Wibberley, C. A. J. (2002), Hydraulic diffusivity of fault gouge zones and implications for thermal pressurization during seismic slip, *Earth Planets Space*, *54*, 1153–1171.

Wibberley, C. A. J., and T. Shimamoto (2003), Internal structure and permeability of major strike-slip fault zones: The Median Tectonic Line in Mie Prefecture, southwest Japan, *J. Struct. Geol.*, *25*, 59–78, doi:10.1016/S0191-8141(02)00014-7.

Wibberley, C. A. J., G. Yielding, and G. Di Toro (2008), Recent advances in the understanding of fault zone internal structure: A review, *Geol. Soc. London Spec. Publ.*, *299*, 5–33, doi: 10.1144/SP299.2.

D. Elsworth and C. Marone, Rock and Sediment Mechanics Laboratory, Center for Geomechanics, Geofluids, and Geohazards, and Energy Institute, Pennsylvania State University, University Park, PA 16802, USA.

J. Samuelson, Faculty of Geosciences, HPT Laboratory, Utrecht University, Budapestlaan 4, Utrecht, NL-3584 CD, Netherlands. (jonesamuelson@gmail.com)